Title

Thermochemical data and phase equilibria of halide (Cl−, Br−, I−) containing AFm and hydrotalcite compounds

Authors

Collin, Marie
Prentice, Dale P
Geddes, Dan
et al.

Publication Date

2024

DOI

10.1111/jace.19665

Thermochemical data and phase equilibria of halide (Cl^-, Br^-, I^-) containing AFm and hydrotalcite compounds

Marie Collin ([,†]), Dale P. Prentice ([*,†]), Dan Geddes ([‡]), John L. Provis ([§]), Kirk Ellison ([**]),*

Magdalena Balonis ([††]), Dante Simonetti ([†,‡‡]), Gaurav N. Sant ([,†,§§,***])*

ABSTRACT

Layered double hydroxides (LDH) phases that form during cement hydration can incorporate a variety of interlayer anions in their interlayer positions. Here, a range of phases of general formula $[M^{II}_{(1-x)}M^{III}_{(x)}(OH)_2][A^{n-}]_{x/n}{\cdot}zH_2O$ were synthesized, where $M^{II} = Mg^{2+}$ (hydrotalcite) or Ca^{2+} (AFm), $M^{III} = Al^{3+}$ such that $[M^{II}/Al] = 2$ (Ca and Mg, atomic units) or 3 (Mg only), and A = Cl^-, Br^-, or I^-. All the synthesized phases were characterized to assess their composition, density, and crystal structure. By approach from undersaturation, the solubility data of these compounds was measured at 5, 25, and 60 °C. This thermochemical data was used to successfully model their formation using thermodynamic modeling, and to infer the fields of stability of these compounds for conditions of relevance to cementitious systems. It is seen that halide-containing hydrotalcites phases strongly compete with hydroxide-containing hydrotalcite, with

[*] Laboratory for the Chemistry of Construction Materials (LC^2), Department of Civil and Environmental Engineering, University of California, Los Angeles, CA, USA
[†] Institute for Carbon Management, University of California, Los Angeles, CA, USA
[‡] Immobilisation Science Laboratory, Department of Materials Science & Engineering, The University of Sheffield, Sheffield, United Kingdom
[§] Paul Scherrer Institut, Forschungsstrasse 111, 5232 Villigen PSI, Switzerland
[**] Electric Power Research Institute, Charlotte, NC, USA
[††] Department of Materials Science and Engineering, University of California, Los Angeles, CA, USA
[‡‡] Department of Chemical and Biomolecular Engineering, University of California, Los Angeles, CA, USA
[§§] Department of Materials Science and Engineering, University of California, Los Angeles, CA, USA
[***] California Nanosystems Institute (CNSI), University of California, Los Angeles, CA, USA

Corresponding authors: M. Collin (Email: mariecollin03@ucla.edu) and G. Sant (Email: gsant@ucla.edu)

the later prevailing at high pH. In contrast, halide-containing AFm compounds are more stable compared to hydroxide-containing AFm compositions.

Keywords: AFm; hydrotalcite; LDH; equilibrium constant; thermodynamic modeling

INTRODUCTION

Cementitious materials based on Portland Cement (PC) present unique advantages for waste immobilization, such as, among others, solid nuclear wastes,[1–4] or concentrated liquid wastes (brines) produced by industrial operations.[5] Often, PC is blended in the binder fraction of a concrete by Supplementary Cementitious Materials (SCMs) to improve properties, including durability, and to reduce the embodied carbon footprint of the concrete binder. As the range of prevalent SCMs expands, so will the types of cementitious hydrates that could form. Typical cementitious hydrates include: calcium-silicate-hydrate (C-S-H), portlandite ($Ca(OH)_2$), ettringite (AFt: alumino-ferrite trisubstituent), or AFm (alumino-ferrite monosubstituent, e.g., monosulfoaluminate) compounds which make up ~90 mass % of a hydrated cementitious formulation.[6,7] Other (non-traditional) hydrated compounds that could form include a range of layered double hydroxide (LDH) compounds. LDH phases are recognizable by their brucite-like structure where a cation located at the center of an octahedron with six hydroxyl groups may be substituted by another cation of a higher valence, inducing the formation of a slightly positively charged layer that requires charge compensation by anions located in the interlayer positions. As such, a typical LDH compounds is represented by the formula $[M^{II}_{(1-x)}M^{III}_{(x)}(OH)_2][A^{n-}]_{x/n}\cdot zH_2O$. When $M^{II} = Ca^{2+}$ and $M^{III} = Al^{3+}$ with Ca/Al = 2, these phases are

commonly referred to as AFm phases and can incorporate a range of anion(s) in their interlayer positions such as SO_4^{2-} (e.g., monosulfoaluminate), CO_3^{2-} (e.g., mono- and hemi-carboaluminate), or Cl^- (e.g., Friedel's and Kuzel's salt).[6,8] When M^{II} = Mg^{2+} and M^{III} = Al^{3+}, with Mg/Al ranging from 2 to 4,[9] the phases belongs to the hydrotalcite-group minerals.[10] Similar to AFm phases, hydrotalcites can incorporate a large range of interlayer anion (e.g., halide anions, carbonates, sulfates, etc.).[9,11–15]

LDH compounds are of interest for anion immobilization in the context of waste management, particularly of liquid wastes.[5] For example, the formation of Friedel's salt during the pozzolanic reaction between a fly ash, portlandite, and Cl-enriched brines was shown to retain a significant fraction of the Cl^- in the solids formed.[16,17] As such, LDH phases could be of interest to retain other less common anions (e.g., other halide anions present as salts in brines or as radionuclides in radioactive wastes). Halide anions may display a competitive behavior: they have been observed to compete for uptake in hydrotalcite phases following in the order $F^- > Cl^- > Br^- > I^-$ [18] or $Br^- > Cl^- > I^-$ [19]. The stability range of these phases is also dependent on the aqueous environment which may induce the formation of other phases instead (e.g., ettringite).[16] It is thus necessary to assess how the presence of halide anions in the interlayer positions of LDH phases affects their solubility and their range of chemical stability. Therefore, in this study, AFm and hydrotalcite (with Mg/Al = 2 and 3) phases containing Cl^-, Br^-, and I^- were synthesized, and characterized compositionally and structurally, using X-ray diffraction, and thermogravimetric (TGA) analysis. In addition, their thermochemical properties (solubility, density) were assessed at 5, 25, and 60 °C. This data assemblage was used to assess the formation and persistence of halide-containing AFm and hydrotalcite-group (henceforth referred to as "hydrotalcites")

compositions in cement-based materials, wherein halide uptake/retention is a matter of importance.

MATERIALS AND METHODS

Hydrotalcite synthesis: For all experiments detailed below, decarbonized deionized water (DIW) was prepared by bubbling N_2 into DIW for an hour prior to using the solution. Hydrotalcite phases (HT) were synthesized in regular atmosphere using a co-precipitation under supersaturation method,[15,18–23] wherein 45 mL of Solution A containing MgX_2 and AlX_3 (where X = Cl, Br, or I) was prepared using pure reagents (>99%) in decarbonated deionized water (DIW) at room temperature under agitation. The target concentrations were 0.8 M MgX_2 and 0.4 M AlX_3 to form hydrotalcites with Mg/Al = 2, and 0.9 M MgX_2 and 0.3 M AlX_3 to form hydrotalcites with Mg/Al = 3. Solution B was prepared at 70 °C using a heating plate by dissolving NaOH in decarbonated deionized water (DIW) so that initial $pH_{70\,°C}$ = 11. Solution A was then added dropwise into 50 mL of Solution B at 70 °C and, and the $pH_{70\,°C}$ was maintained in the range 11-12 by periodic introduction of 10 M NaOH over the course of the reaction. The final slurries were aged under agitation for 1 hour at 70 °C in hermetically sealed Pyrex glass bottles to prevent carbonation. The solids were separated from the solutions by centrifugation and washed multiple times with hot decarbonated DIW until the pH of the leachate stabilized at a near-neutral value. The solids were then vacuum filtered and carefully dried in an inert atmosphere (N_2) at 50 °C. Note that, due to the impossibility to perform the synthesis and to separate the solid from the solution in an inert atmosphere, some carbonation of the slurries may have occurred prior to the drying step.

AFm synthesis: AFm phases were synthesized in regular atmosphere following a typical protocol,[6,8,24–26] $Ca_3Al_2O_6$ (C_3A – synthesized by thoroughly grinding a 3:1 molar ratio mixture of pure reagent grade $CaCO_3$ and Al_2O_3 and heating the powder at 1350 °C for 3 hours)[25] was mixed with pure (>99%) CaX_2 (where X = Cl, Br, or I) on a 1:1 molar ratio in decarbonated DIW at a liquid-to-solid (l/s, mass basis) of 10. The slurries were agitated for 28 days at 25 °C in hermetically sealed Polytetrafluoroethylene (PTFE) bottles to prevent carbonation. The solids were separated from the solutions after 28 days by vacuum filtration, rinsed with DIW, vacuum filtered, and then carefully dried in an inert atmosphere (N_2) at 50 °C. As was the case for the HT phases, some carbonation of the slurries may have occurred prior to the drying step.

Solid composition analysis: A small fraction of each solid (5 mg) was dissolved in acidic media (200 mL, pH 0-3) to determine the composition of the synthesized phases. 0.01 vol% sulfuric acid (ACS grade) was used for anion (Cl^-, Br^-, or I^-) concentration measurement using ion chromatography (IC) (Dionex™ Integrion™ HPIC™ System equipped with a Dionex IonPac AS19 Column). 5 vol% nitric acid (trace-metal grade) was used for cation (Mg^{2+} or Ca^{2+}) measurement using inductively coupled plasma - optical emission spectrometry (ICP-OES) using a Perkin Elmer Avio 200 instrument. 5 vol% nitric acid (trace-metal grade) was used for Al^{3+} measurement using inductively coupled plasma – mass spectrometry (ICP-MS) using a Perkin Elmer NexION 2000 instrument. All results were converted to molar concentration units from a calibration curve prepared with standard solutions (Inorganic Ventures) and combined to estimate the elemental composition. In all cases, a blank sample corresponding to pure 0.01 vol% sulfuric or pure 5 vol% nitric acid was analyzed to assess the level of contamination of the acids.

Thermogravimetric analysis: Thermogravimetric analysis (TGA) was performed using a Perkin Elmer STA 6000 and/or a Perkin Elmer TGA4000 under a flow of ultrapure nitrogen in an aluminum oxide crucible. A heating ramp of 10 °C/min was used between 35 and 950 °C, after 5 min equilibration at 35 °C for temperature consistency. The thermogravimetric mass loss (TG) and the derivative mass loss (DTG) were both used to quantify the amount of physically and chemically-bound water.[27,28]

X-Ray diffraction: XRD analysis was performed using a PANalytical X'Pert pro diffractometer (θ-θ configuration, CuKα radiation, λ = 1.54 Å) on powdered samples provided with textured surfaces to minimize the potential for preferred orientation. Scans were acquired between 5° and 70° with a step-size of 0.02° using an X'Celerator 2 detector. The crystal unit cell parameters were refined using Celref for powder samples spiked with ~10 mass % of ZnO (99.999%) as a reference to ensure accurate peak positions.[29]

Multipycnometry: The solid density was measured using helium pycnometry (AccuPyc II 1340, Micrometrics). Around 0.5 g of sample was used for each measurement. A cyclical helium flush procedure was set to repeat until stable vacuum pressure (degas stage) was achieved, at which point ten data points were collected via additional helium purges.

Solubility measurements: ~300 mg of the solid was dispersed in 10 mL of DIW and left under agitation in tightly closed PTFE containers to prevent carbonation for 4 months at 5, 25, and

60 °C in environmental chambers and in regular atmosphere. The final pH of the slurry was measured prior to solid-leachate separation. The AFm-containing slurries were passed through a 0.2 µm nylon filter to separate the solid from the solution. The HT-containing slurries were filtered using centrifugal ultrafiltration (polyethersulfone membrane for concentration, 100 kDa molecular weight cutoff: MWCO) to separate the very fine particulates (d_{50} = 0.17 ± 0.04 µm) from the solution. In both cases, part of filtrate was diluted in a 5 vol% nitric acid matrix to ensure the stability of the solution prior to Mg, Ca, and Al measurement as detailed in the *Solid composition analysis* section. The rest of the filtrate was diluted in a 0.01 vol% sulfuric acid matrix to ensure the stability of the solution prior to anion (Cl^-, Br^-, or I^-) measurement as detailed in the *Solid composition analysis* section. The filtered solids were dried in an inert atmosphere at 60 °C for 24 h and analyzed using XRD as noted above to evaluate the phase composition/structure.

Calculation of the solubility constants and thermochemical data: The solubility constants ($\log K_{SO}$) of the phases of interest were calculated at 5, 25, and 60 °C based on: (1) the solid composition and (2) the leachate composition using Equation 1 (AFm phases) or Equation 2 (HT phases) as appropriate:

$$K_{so} = a_{H_2O}^{y} \cdot a_{Ca^{2+}}^{m} \cdot a_{AlO_2^-}^{a} \cdot a_{X^-}^{x} \cdot a_{OH^-}^{h} \quad \text{(X = } Cl^-, Br^-, \text{ or I-)} \quad \text{Equation 1}$$

$$K_{so} = a_{H_2O}^{y} \cdot a_{Mg^{2+}}^{m} \cdot a_{AlO_2^-}^{a} \cdot a_{X^-}^{x} \cdot a_{OH^-}^{h} \quad \text{(X = } Cl^-, Br^-, \text{ or I-)} \quad \text{Equation 2}$$

where K_{SO} is the solubility constant, $a_{H_2O}^{y}$ is the activity of water with y as its stoichiometric coefficient, and a_i^* is the activity of a given ionic species and * its stoichiometric coefficient (where * represents y, m, a, x, or h).

Knowing K_{SO} at 298.15 K, the Gibbs energy of formation at standard conditions ($\Delta_f G_{298}^{\circ}$ defined at 298.15 K and 1 bar) of the phases of interest was calculated using Equation 3:[30]

$$\Delta_f G_{298}^0 + \sum_i v_i \Delta_f G_T^0 = -RTln(K_{SO}) \quad \text{Equation 3}$$

where v_i is the stoichiometric reaction coefficient, $\Delta_f G_T^0$ is the Gibbs energy of formation of the ionic species detailed in Equation 1 (refer to **Table S1** for the values)[31,32], R is the gas constant (8.314 J/(mol·K)), and T is the temperature in K. The standard absolute isobaric heat capacity (Cp_{298}°) and the entropy of reaction (S_{298}°) were estimated following the reference reactions (see **Table S1**)[31,33–39] and assuming that $\Delta_r S$ = 0 (see equation 62 detailed by Helgeson)[34] and $\Delta_r C_p$ = 0 (see equation 78 detailed by Helgeson)[34]:[9,15,34,40]

AFm phases

$$\mathrm{Ca_4Al_2(SO_4)(OH)_{12}\cdot 6H_2O + 0.5CaSO_4 + CaX_2} \rightarrow \mathrm{Ca_4Al_2X_2(OH)_{12}\cdot 3H_2O + 1.5CaSO_4\cdot 2H_2O} \quad \text{Equation 4}$$

X = Cl^-, Br^-, or I^-

HT phases

$$\mathrm{7.71Mg_{0.74}Al_{0.26}(CO_3)_{0.13}(OH)_2\cdot 0.39H_2O} + \left[\frac{(z+2a-21.38)}{2}\right]\mathrm{Mg(OH)_2} + \left[\frac{y}{2}\right]\mathrm{MgCl_2} \rightarrow \mathrm{Mg_xAl_2X_y(OH)_z\cdot aH_2O + MgCO_3} + \left[x - 5.69 - \frac{(z+2a-21.38)}{2} - \frac{y}{2} - 1\right]\mathrm{MgO} \quad \text{Equation 5}$$

X = Cl^-, Br^-, or I^-

The enthalpy of reaction ($\Delta_r H^0_{T_0}$) and the entropy of reaction ($\Delta_r S^0_{T_0}$) are interdependent via the Gibbs free energy:[30]

$$\Delta G = \Delta H - T\Delta S \qquad \text{Equation 6}$$

Thermodynamic modeling: Thermodynamic modeling was carried out using GEM-Selektor v.3.6 (GEMS)[41,42] which incorporates the slop98.dat and Cemdata18 thermodynamic databases.[32,35,43,44] To represent the non-ideality of the solutions, the activity coefficients were calculated using the Truesdell-Jones extension to the Debye-Hückel equation that is applicable for I_m ≈ 2 mol/L (i.e., an ionic strength range encompassing all the systems studied herein):[45]

$$\log_{10}\gamma_i = \frac{-A_\gamma z_i^2\sqrt{I}}{1 + \dot{a}B_\gamma\sqrt{I}} + b_\gamma I + \log_{10}\frac{X_{jw}}{X_w} \qquad \text{Equation 7}$$

where γ_i is the activity coefficient and z_i the charge of the i^{th} aqueous species, A_γ and B_γ are temperature, and pressure-dependent coefficients, X_{jw} is the molar quantity of water, X_w is the total molar amount of the aqueous phase, and I is the molal ionic strength. A common ion size parameter ($a = 3.72$ Å) and a short-range interaction parameter ($b_\gamma = 0.64$ kg mol^{-1}) were used, assuming NaCl is the background electrolyte.[45,46]

RESULTS AND DISCUSSION

Phase characterization:

The X-ray diffractograms of the synthesized solids, displayed in Figure 1a, are characteristic of the rhombohedral structure typically observed for hydrotalcite-group phases,[15,47,48] and some AFm phases (e.g., hemicarboaluminate, "high temperature" Cl-AFm, etc.).[8] In contrast, the Cl-AFm structure is monoclinic: the transition from monoclinic to rhombohedral is observed

around 35 °C,[49] i.e., in between the temperature of synthesis and drying used here, which indicates that the phase formed during synthesis either remained stable during the drying, or reverted back to a monoclinic structure when stored at room temperature. No crystalline $Mg(OH)_2$, $Ca(OH)_2$, or $Al(OH)_3$ was detected. The three AFm phases show a much higher degree of crystallinity compared to the hydrotalcite phases: the AFm phases display very narrow, well-defined peaks, while those of the hydrotalcites are much broader, indicative of poor crystallinity. In all cases (AFm and HT), a shift in the first peak position to lower 2Θ values is observed with increasing intercalant anion size – considering nanoconfined anions with one hydration shell[50] – following the order Cl^- (3.19 Å)[51] < Br^- (3.37 Å)[51] < I^- (3.65 Å)[51] (Figure 1b). This shift is related to an increase of the interlayer spacing to accommodate the hydrated anion, which affects the entire crystal structure (Figure 1c).[19,52] In addition, a broadening of the peaks (i.e., decreasing crystallinity) is observed with increasing anion size and, in the case of the I-HT phase, a peak slitting is observed, with the second peak observed at ~11.5 °2Θ for both the I-HT2 and I-HT3 phases. Similar splitting has been observed in the literature for poorly crystalline phases and is typically attributed to carbonate impurities.[9] However, little to no carbonate is incorporated in these phases, as confirmed by TGA analysis (Table 2). The split observed here likely indicates the presence of mixed OH-HT and I-HT phases instead, as the 003-peak position for OH-HT2 phase has been observed at 11.52 °2Θ in the literature.[9] This suggests that, while a solid solution may form between I-HT and OH-HT phases, there is a miscibility gap at high I/(I+OH) ratio. A solid solution is typically favored when the anions are similar in size, shape, and form.[8,53] Here, I^- is the largest of the three anions studied, and the one that most differs from OH^- in terms of bare ionic radius (1.32 to 1.37 Å depending on the

coordination number for OH^-,[54] 2.20 Å for I^- [55]). This may indicate a phase separation rather than the formation of a highly non-ideal solid solution at high I/(I+OH) ratio, such that a mixture of OH-HT and I-HT shows a 2-peak signal.

Rhombohedral phases display a cell structure where $a = b \neq c$, and $\alpha = \beta = 90°$ and $\gamma = 120°$. Here, *a* (and *b*) remains constant within error regardless of the intercalant anion (Table 1). This is consistent with previous observations that showed that *a* is not affected by the anion type for both AFm[56] and hydrotalcite phases[15] and, for hydrotalcites, is minimally affected by the Mg/Al ratio. In contrast, the *c* parameter shows a constant increase with increasing anion radius (Figure 1c). Such an increase is consistent with previous observations across monovalent and divalent anions such as halides, carbonates, sulfates, nitrates, etc.[9,15,18,52] Of note, the *c* parameter of hydrotalcite phases shows a slight variation as a function of the Mg/Al ratio, as the larger ionic radius of Mg^{2+} compared to Al^{3+} results in a larger unit cell;[57] but this variation is negligible compared to the effect induced by the intercalant anion. All values observed (*a* and *c* parameters, Table 1) are consistent with previous observations in the literature.[9,19,47,56,58–64]

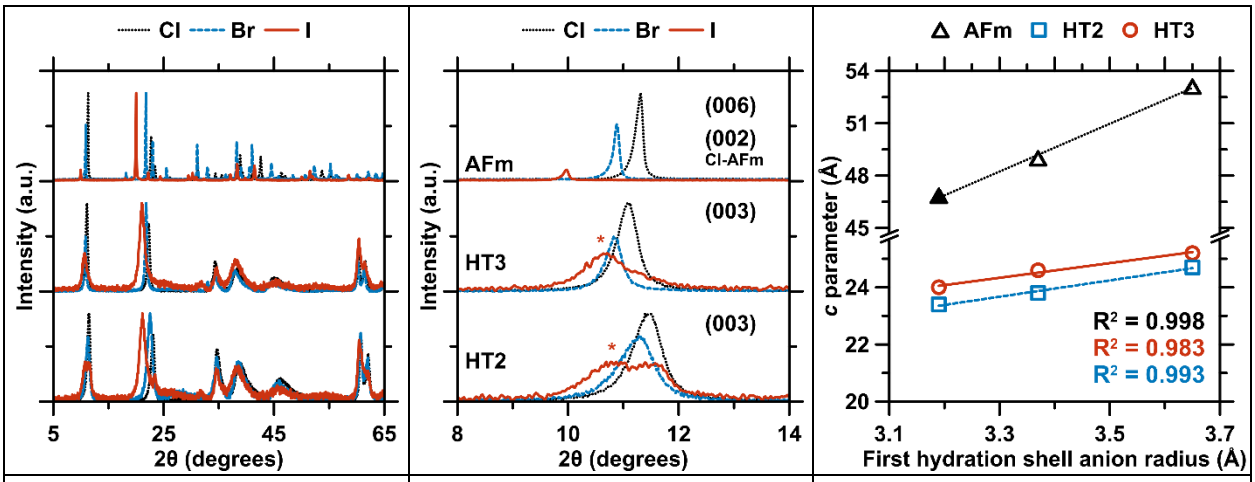

Figure 1. XRD analysis of the phases synthesized. **(a)** Their XRD reflections, and **(b)** a magnification of the first peak. **(c)** The calculated *c* parameter for all synthesized phases of interest as a function of the anionic radius (Cl^- = 1.81 Å, Br^- = 1.96 Å, I^- = 2.20 Å)[65,55]. Note that, for the I-containing hydrotalcite phases, only the major phases (highlighted with the * symbols in figure b) were considered for the crystal structure parameters calculation as displayed in figure c and Table 1. The error bars associated to the *c* parameters (**Table 1**) are smaller than the size of symbols used and are not displayed here. The *c* parameter of the rhombohedral form of Cl-AFm (46.849 Å) is taken from Renaudin et *al*.[49]

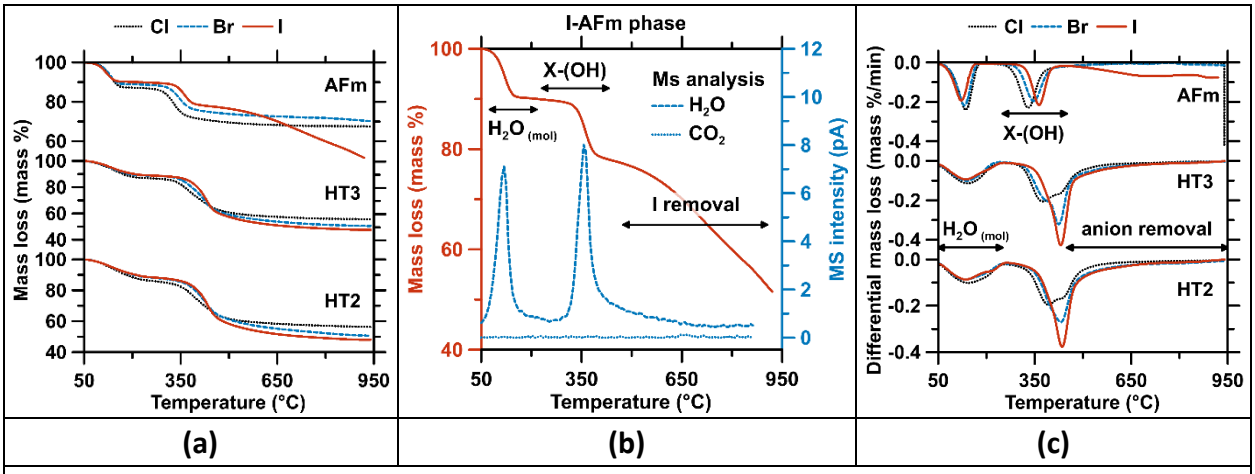

Figure 2. Thermogravimetric analysis data obtained for all synthesized solids. **(a)** The mass loss as a function of temperature for all phases. **(b)** A comparison between the mass loss and the H_2O and CO_2 signals detected by GC-MS during the analysis of the gas generated during I-HT2 phase decomposition. **(c)** The differential mass loss as a function of temperature for all phases and their attribution.

Table 1. The density and unit cell parameters of the samples within the rhombohedral symmetry (R3c, $a = b \neq c$, $\alpha = \beta = 90$ °, $\gamma = 180$ °) or the monoclinic symmetry (C2/c, $a \neq b \neq c$, $\alpha = \gamma = 90$ °).

Rhombohedral structures

The *c* parameter values marked with * were calculated assuming a rhombohedral structure where *c* = 3 x interlayer spacing.

	***a*-parameter**		***c*-parameter**		**Density**	
Phase	**This study**	**Literature**	**This study**	**Literature**	**This study**	**Literature**
Cl-HT2	3.05 ± 0.02	3.04 [58]	23.4 ± 0.1	~23.5 *[9]	1.98 ± 0.01	-
Cl-HT3	3.07 ± 0.02	3.06 [59], 3.07 [47]	24.0 ± 0.2	23.90 [47]	1.94 ± 0.01	-
Br-HT2	3.05 ± 0.02	3.04 [58]	23.8 ± 0.1	-	2.14 ± 0.01	-
Br-HT3	3.07 ± 0.02	3.06 [59], 3.07 [47]	24.6 ± 0.1	~24.4 *[19]	2.11 ± 0.01	-
I-HT2	3.05 ± 0.02	3.04 [58]	24.7 ± 0.2	-	2.17 ± 0.01	-
I-HT3	3.06 ± 0.02	3.06 [59], 3.07 [47]	25.2 ± 0.1	~25.2 *[19]	2.15 ± 0.01	-
Br-AFm	5.76 ± 0.02	5.76 [66,67]	49.0 ± 0.1	48.108 [61], 49.12 [66]	2.22 ± 0.01	-
I-AFm	5.78 ± 0.02	5.77 [61,63]	53.2 ± 0.1	26.538 (R3) [61], 53.10 (R3c) [63]	2.31 ± 0.01	-

Monoclinic structure

	***a*-parameter**		***b*-parameter**		***c*-parameter**		***β*-parameter**		**Density**	
Phase	**This study**	**Literature**	**This study**	**Literature**	**This study**	**Literature**	**This study**	**Literature**	**This study**	**Literature**
Cl-AFm	9.97 ± 0.05	9.979 [68]	5.75 ± 0.02	5.751 [68]	16.32 ± 0.06	16.320 [68]	104.7 ± 0.6	104.53 [68]	2.05 ± 0.01	2.06 [60]

All HT and AFm phases show two major mass losses below 250 and 450 °C (Figure 2a), and I- and Br-containing phases show additional mass loss above 450 °C. Mass spectrometry of the evolved gas shows that the first two mass losses are related to water loss (see Figure 2b for the I-AFm signals as an example). The additional mass losses are uncorrelated to H_2O, and CO_2 removal is minimal in all cases (Table 2), thus the additional mass losses can be attributed to the intercalant anion vaporization (note that the anion could not be analyzed with the device used here).[63,69] The first water mass loss (<250 °C, Figure 2c) is typically attributed to poorly bound water molecules that are removed from the interlayer spacing, while the second water mass loss (250 < T < 850 °C) is associated to tightly bound water molecules, and recondensation of hydroxyl groups. The second water loss peak has been observed to overlap with the removal of some interlayer anion species.[9,63] Here, the water signal from MS analysis was used to separate the water contribution from the anion contribution to the mass loss around 450 °C.[70] The mass losses related to poorly and tightly bound water molecules, and hydroxyl group recondensation, are compiled in Table 2. The total water content recorded for the AFm phases is consistent with the content expected from the theoretical formulas and previously measured experimentally.[27,61,62,66] The total water content recorded for the HT-phases follows the trend of increasing water amount with increasing Mg/Al ratio typically observed for hydrotalcite (Figure S1).

Table 2. The mass loss established via TGA analysis of the synthesized solids (hydrotalcite and AFm) following a careful drying procedure in an inert atmosphere (N_2) at 50 °C to prevent phase carbonation.

	Content (mass %)				
Phase	**H_2O molecular (Mass loss 1: 50-250 °C)**	**H_2O hydroxyl groups (Mass loss 2: 250-450 °C)**	**Total water mass loss (50-450 °C)**	**CO_2 mass loss (450-850 °C)**	**Anion mass loss (250-450 °C)**
Cl-HT2	13.7	23.7	37.4	0.7	5.2
Cl-HT3	13.2	25.0	38.2	0.8	5.2
Br-HT2	11.6	21.8	33.4	0.8	14.4
Br-HT3	11.1	25.4	36.5	0.8	11.7
I-HT2	11.4	23.6	35.0	0.9	15.6
I-HT3	10.4	22.7	33.0	1.2	17.8
Phase	**H_2O molecular (Mass loss 1: 50-200 °C)**	**H_2O hydroxyl groups (Mass loss 2: 200-450 °C)**	**Total water mass loss (450-850 °C)**	**CO_2 mass loss (450-850 °C)**	**Anion mass loss (450-850 °C)**
Cl-AFm	12.8	16.8	29.6	0.5	N.D.
Br-AFm	11.1	14.3	25.3	0.6	0.7
I-AFm	9.9	12.5	22.4	0.6	15.5

The elemental composition, as determined via solid dissolution (acid digestion), was combined with the water quantity as determined by TGA to establish the composition of the solids as detailed in Table 3. The AFm compositions are perfectly consistent with the expected stoichiometry ($Ca_4Al_2(OH)_{12}X_2 \cdot 3H_2O$ with X = Cl^-, Br^-, or I^-). The Mg/Al ratios of the hydrotalcite phases are noted to be higher than expected from the starting solution composition. This is because hydrotalcite phase stability changes with pH: higher Mg/Al ratio are favored at higher pH, as will be discussed below. In addition, in the case of the I-containing hydrotalcite phase, the I/Al ratio is lower than the expected value of 1, while for the other phases the anion/Al ratio is in the range of 1. This is consistent with the split 003 peak observed in Figure 1b attributed to the formation of mixed I/OH-containing hydrotalcite phases.

Table 3. The solid compositions determined for each phase, and the dissolution reactions used to calculate the solubility constants of the hydrated phases.

Identifier	Mg/Al	Anion/Al	Dissolution reaction (of synthesized molar compositions)
Cl-HT2	2.5	1.1	$Mg_{5.0}Al_2(OH)_{13.8}Cl_{2.2}\cdot 5.2H_2O \rightleftharpoons 5.0Mg^{2+} + 2AlO_2^- + 2.2Cl^- + 5.8OH^- + 9.2H_2O$
Cl-HT3	3.6	1.1	$Mg_{7.1}Al_2(OH)_{18.0}Cl_{2.2}\cdot 6.4H_2O \rightleftharpoons 7.1Mg^{2+} + 2AlO_2^- + 2.2Cl^- + 10.0OH^- + 10.4H_2O$
Br-HT2	2.7	1.1	$Mg_{5.4}Al_2(OH)_{14.6}Br_{2.2}\cdot 6.0H_2O \rightleftharpoons 5.4Mg^{2+} + 2AlO_2^- + 2.2Br^- + 6.6OH^- + 10.0H_2O$
Br-HT3	3.9	0.9	$Mg_{7.8}Al_2(OH)_{19.8}Br_{1.8}\cdot 7.7H_2O \rightleftharpoons 7.8Mg^{2+} + 2AlO_2^- + 1.8Br^- + 11.8OH^- + 11.7H_2O$
I-HT2	3.2	0.7	$Mg_{6.4}Al_2(OH)_{17.4}I_{1.4}\cdot 7.2H_2O \rightleftharpoons 6.4Mg^{2+} + 2AlO_2^- + 1.4I^- + 9.4OH^- + 11.2H_2O$
I-HT3	4.0	0.6	$Mg_{8.0}Al_2(OH)_{20.8}I_{1.2}\cdot 5.1H_2O \rightleftharpoons 8.0Mg^{2+} + 2AlO_2^- + 1.2I^- + 12.8OH^- + 9.1H_2O$
Identifier	**Ca/Al**	**Anion/Al**	**Dissolution reaction (of synthesized molar compositions)**
Cl-AFm	2.0	1.0	$Ca_4Al_2(OH)_{12}Cl_2\cdot 3H_2O \rightleftharpoons 4Ca^{2+} + 2AlO_2^- + 2Cl^- + 4OH^- + 7H_2O$
Br-AFm	2.0	1.0	$Ca_4Al_2(OH)_{12}Br_2\cdot 3H_2O \rightleftharpoons 4Ca^{2+} + 2AlO_2^- + 2Br^- + 4OH^- + 7H_2O$
I-AFm	2.0	1.0	$Ca_4Al_2(OH)_{12}I_2\cdot 3H_2O \rightleftharpoons 4Ca^{2+} + 2AlO_2^- + 2I^- + 4OH^- + 7H_2O$

Solubility measurements

The proposed dissolution reactions are compiled in Table 3. Note that, in all cases (HT and AFm), the dissolution reaction after 5 months of equilibration in DIW at 5, 25, and 60 °C was incongruent due to the precipitation of $Al(OH)_3$, as attested by (1) the solution composition (Supplementary Information: Figure S2a and Table S2), and (2) post-dissolution XRD analysis of the solids (Supplementary Information: Figure S3). However, no $Ca(OH)_2$ or $Mg(OH)_2$ were detected in the post-dissolution XRD solid patterns, and all Mg (Supplementary Information: Figure S2b) and Ca concentrations (Supplementary Information: Figure S2c) are below the solubility limit of $Ca(OH)_2$ or $Mg(OH)_2$ at their respective temperature. The activities and speciation of the aqueous components were calculated using GEMS from the solution compositions detailed in Supplementary Information: Table S2 and used to calculate $\log K_{SO}$ using Equation 1 (AFm phases) or Equation 2 (HT phases), respectively.

The $\log K_{SO}$ values of the three AFm phases synthesized here are similar to prior observations[8,63] (Figure 3a). Note that here, the error associated with the solubility constants was calculated via error propagation analysis (EPA: refer to Table S3 for more information) in addition to simply considering the uncertainty arising from the solution concentration measurements, which is approximately ± 1.2 log units. Unsurprisingly, the uncertainty estimated by the EPA is much larger than the values typically reported in the literature. The $\log K_{SO}$ increases with temperature as typically observed in the literature.[6,8,30] The $\Delta_r S^0_{T_0}$ values calculated with Equation 4 (marked as "Additivity" in Figure 3) do not provide a perfect fit to the temperature

dependence of the experimental logK_{SO} values gathered here, but the fit lie well within the uncertainty of the measurements.

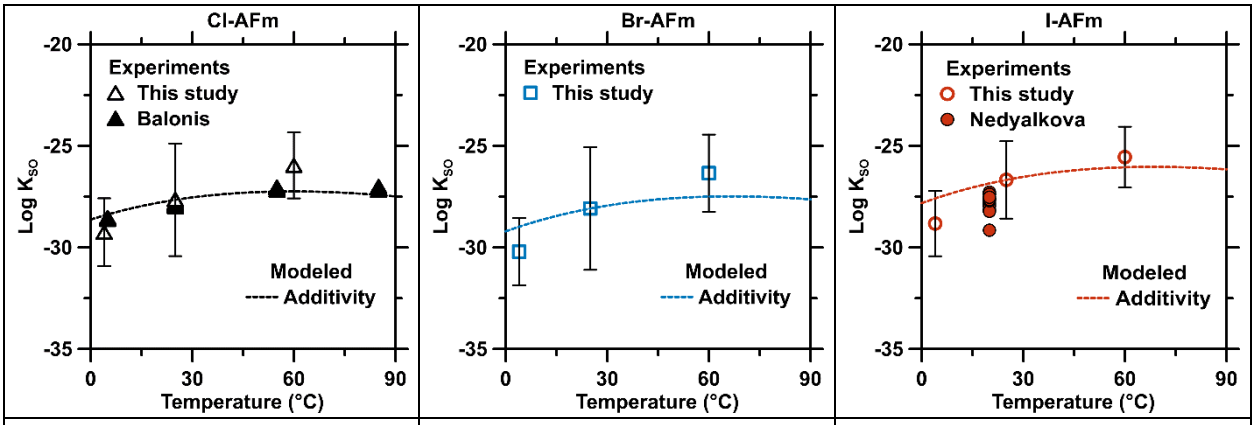

Figure 3. The solubility constants (logK_{so}) of the synthetic AFm phases synthesized herein or from the literature[8,63] as a function of temperature. The lines represent conditions where $\Delta_r S^0_{T_0}$ is calculated using the additivity equation (Equation 4). The uncertainty in the solubility constants calculated via error propagation analysis is substantial (see **Table S3**). More practically, the uncertainty in the solubility constant based on the uncertainty in solution concentrations alone is more modest, and on the order of ±1.2 log units.

For hydrotalcite phases, the logK_{SO} values follow a linear relationship as the function of the Mg/Al ratio regardless of the temperature (Figure 4a to c), as previously observed in the literature.[9] As is the case with the AFm phases, the $\Delta_r S^0_{T_0}$ values calculated with Equation 5 do not provide a perfect fit of the experimental logK_{SO} data (Figure 5), although it remains in the uncertainty of the measurement. In general, the solubility constants diverge from the calculated trends with increasing higher temperature, especially for HT3 phases (Figure 5d to f). As per literature observations, the solubility of hydrotalcite phases remains relatively flat across the 0-to-60 °C temperature range.[9] Contrastingly, for the Br, I and Cl-HT phases studied herein logK_{SO} increases substantively with temperature, indicating a higher solubility of HT at higher temperatures. The discrepancies observed between the trends observed here and that of the

literature may be because Mg concentrations in the literature have inferred from the solubility limit of brucite – $Mg(OH)_2$ – as the experimental concentrations were lower than the instrumental detection limit.[9] This may induce uncertainty in the logK_{SO} values calculation as $Mg(OH)_2$ solubility is strongly affected by temperature.

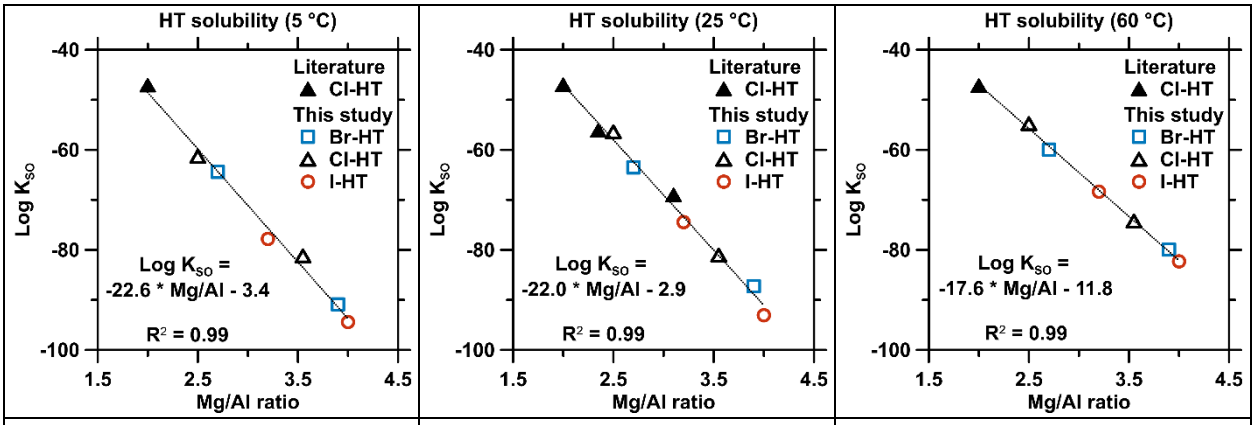

Figure 4. The linear relationship observed between the experimental logK_{SO} and the Mg/Al ratio of the HT phases measured here and from the literature[9,18,48] at (a) 5, (b) 25, and (c) 50 °C. The uncertainty in the solubility constants calculated via error propagation analysis is substantial (see Table S3). More practically, the uncertainty in the solubility constant based on the uncertainty in solution concentrations alone is much more modest, and on the order of ±0.9 (HT2) and ±1.2 (HT3) log units.

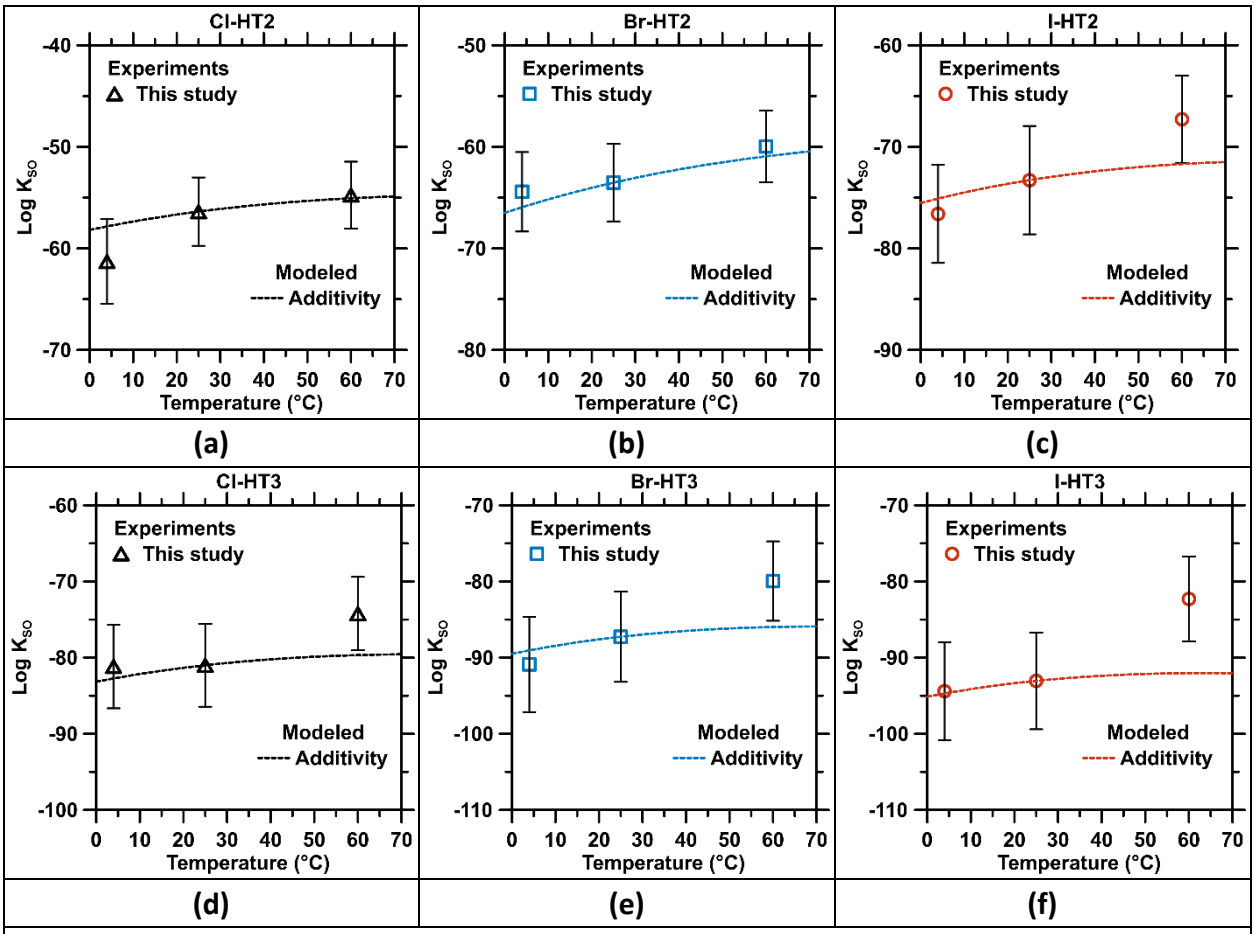

Figure 5. The experimental logK_{so} of the synthetic HT phases – plotted as symbols in the figures – as a function of temperature. The lines represent conditions where $\Delta_r S^0_{T_0}$ is calculated using the additivity equation (Equation 5). The uncertainty in the solubility constants calculated via error propagation analysis is substantial (see Table S3). More practically, the uncertainty in the solubility constant based on the uncertainty in solution concentrations alone is much more modest, and on the order of ±0.9 (HT2) and ±1.2 (HT3) log units.

Thermodynamic modeling of hydrated phase formation

The tabulated thermochemical data are displayed in Table 4. In general, the S_{298}° values and the Cp_{298}° values derived from Equation 4 (AFm phases) or Equation 5 (HT phases) are well correlated to the experimental molar volume of the phases derived from the experimental molar mass and the experimental density, following a trend consistent with that observed for similar type of phases (Figure S4). The thermochemical data was used to model the solubility of all phases of interest.

The modeled results for the AFm phases are compared to experimental results obtained here and from the literature[8,63] in Figure 6a-d. In general, a good agreement of the trends is observed between the model and experimental solubilities (Figure 6d). Note that the solubility of the I-AFm phase studied herein does not cover the range observed by Nedyalkova et *al.*[63,64] wherein I-AFm is still observed to form up to pH 13 – alongside katoite – within a solid solution: increasing OH^- incorporation is observed in the I-AFm phase with increasing pH. The existence of a solid solution needs to be accounted for to fully assess the stability of the I-AFm phase at higher pH. A similar increasing OH^- incorporation with increasing pH has been reported for the Cl-AFm,[71] and may thus be expected for the Br-AFm phase, highlighting potential limitations of the solubility products proposed here at higher pH. The modeled results for the HT phases are compared to experimental results obtained here and from the literature in Figure 7a-d. A reasonable agreement is observed for most systems, between the model and experimental solubilities. The differences observed (see Figure 7d) implicate datasets with uncertain pH values due to the limited availability of solution data (e.g., Figure 7c), and low anion concentrations. This suggests that, in the experimental systems, anion leaching may have

occurred from the solids, in addition to hydrotalcite dissolution. Thus, the simulations may over-predict anion uptake into the solid phase(s). Nevertheless, the good agreement between experimental and modeled Mg and Al concentrations still validates the thermodynamic attributes calculated here.

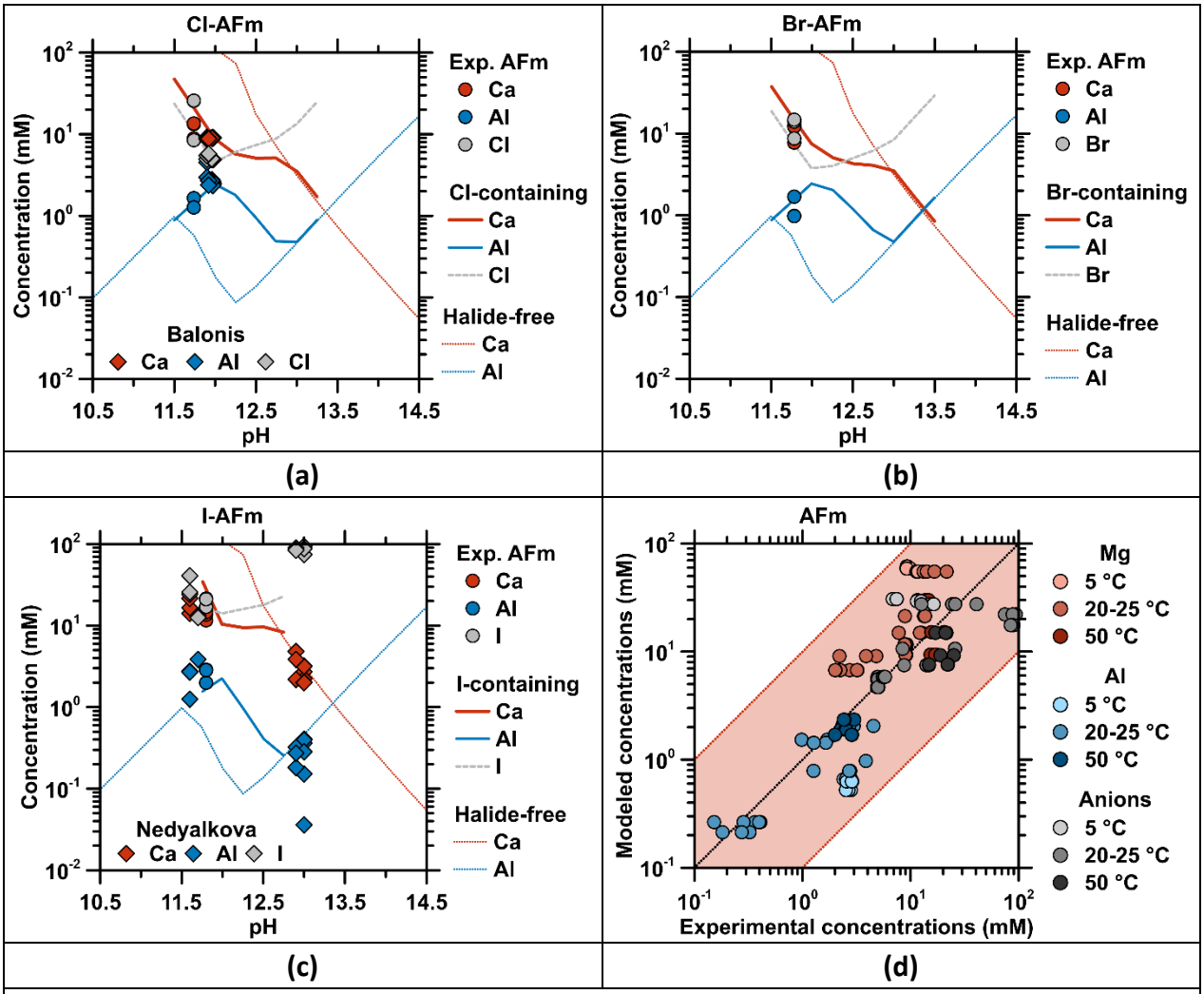

Figure 6. The experimental and modeled solubilities at 25 °C for: **(a)** Cl-AFm (additional experimental data was taken from Balonis et *al*.[8]), **(b)** Br-AFm, and **(c)** I-AFm phases (additional experimental data was taken from Nedyalkova et *al*.[63]) synthesized here. Shown herein are the modeled aqueous compositions, including those for the CaO-Al_2O_3-H_2O system comprising katoite (C_3AH_6), $Ca(OH)_2$ and $Al(OH)_3$ (microcrystalline) as implemented in GEMS. **(d)** Direct comparison between experimental and modeled concentration for a temperature range of 5-to-60 °C. The black dashed line is y = x. The area in red signifies $10^{\pm1}$ of y = x. The error bars associated to the standard deviation of the elemental concentrations are smaller than the size of symbols used and are not displayed here.

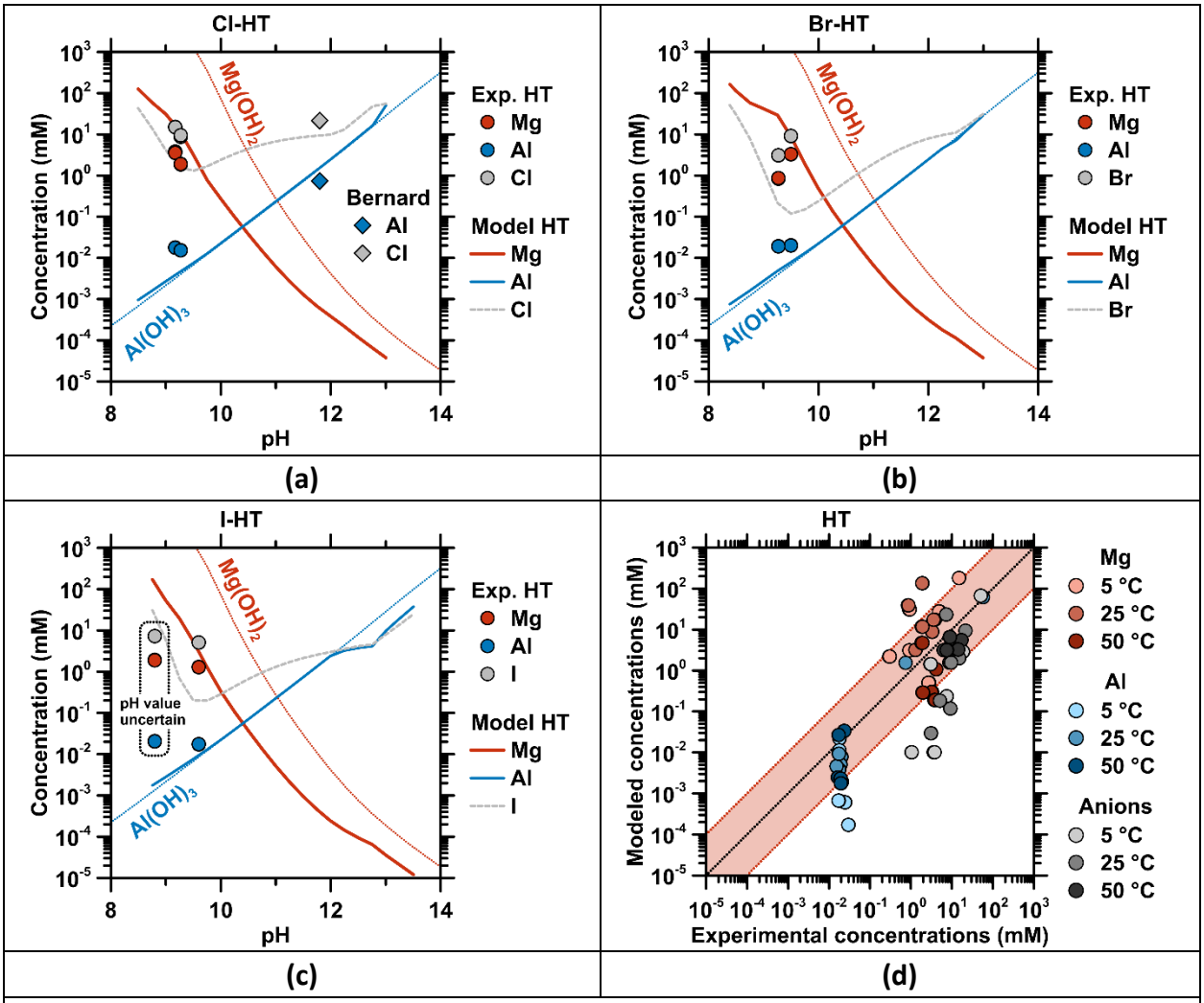

Figure 7. The experimental and modeled solubilities at 25 °C for: **(a)** Cl-HT (Additional experimental data was taken from Bernard et *al.*[9]), **(b)** Br-HT, and **(c)** I-HT phases synthesized herein. Shown herein are the modeled aqueous compositions, including those for $Mg(OH)_2$ and $Al(OH)_3$ (microcrystalline) as implemented in GEMS. **(d)** Direct comparison between experimental and modeled concentration for a temperature range of 5-to-60 °C. The black dashed line is y = x. The area in red signifies $10^{\pm 1}$ of y = x. The error bars associated to the standard deviation of the elemental concentrations are smaller than the size of symbols used and are not displayed here.

Table 4. Thermochemical data of the different AFm and H-T compounds at T = 25°C and p = 1 bar. $V°_{(1)}$ is calculated from the experimental density (Table 1) and phase composition. $V°_{(2)}$ and its corresponding density are estimated from the crystal cell parameters inferred from the XRD pattern (Table 1). The $\Delta_f H^\circ_{298}$, S°_{298}, and Cp°_{298} values were inferred from Equation 4 (AFm phases) or Equation 5 (HT phases). The estimated error for all attributes is ± 10%.

Identifier	**Chemical Formula**	$V°_{(1)}$	$V°_{(2)}$	**Density** (2)	logK_{so}	$\Delta_f G^\circ_{298}$	Cp°_{298}	$\Delta_f H^\circ_{298}$	S°_{298}
		(cm^3/mol)	(cm^3/mol)			(kJ/mol)	(J/mol/K)	(kJ/mol)	(J/mol/K)
Cl-HT2	$Mg_{5.0}Al_2(OH)_{13.8}Cl_{2.2}·5.2H_2O$	293.3	260.5	2.2	-56.4	-7629.8	806.0	-8607.2	720.9
Cl-HT3	$Mg_{7.1}Al_2(OH)_{18.0}Cl_{2.2}·6.4H_2O$	373.7	270.1	2.7	-81.0	-9668.8	1016.3	-10862.7	896.9
Br-HT2	$Mg_{5.4}Al_2(OH)_{14.6}Br_{2.2}·6.0H_2O$	335.2	266.0	2.7	-63.5	-8107.8	871.3	-9035.7	805.5
Br-HT3	$Mg_{7.8}Al_2(OH)_{19.8}Br_{1.8}·7.7H_2O$	408.7	277.1	3.1	-87.3	-10512.2	1125.6	-11878.2	1007.8
I-HT2	$Mg_{6.4}Al_2(OH)_{17.4}I_{1.4}·7.2H_2O$	375.3	279.0	2.9	-74.4	-9192.8	999.4	-10392.4	897.8
I-HT3	$Mg_{8.0}Al_2(OH)_{20.8}I_{1.2}·5.1H_2O$	393.4	285.1	3.2	-93.0	-10051.7	1039.2	-11250.0	916.3
Cl-AFm	$Ca_4Al_2(OH)_{12}Cl_2·3H_2O$	265.0	363.9	1.49	-27.7	-6575.9	791.8	-7236.7	658.8
Br-AFm	$Ca_4Al_2(OH)_{12}Br_2·3H_2O$	285.1	324.6	1.95	-28.1	-6523.9	793.9	-7123.7	684.2
I-AFm	$Ca_4Al_2(OH)_{12}I_2·3H_2O$	313.8	351.6	2.07	-26.7	-6411.6	796.1	-6977.7	699.5

The thermochemical data were used to further study the stability of the various systems (hydrotalcite and AFm). The hydrotalcite phases all display a similar trend where lower Mg/Al ratios are favored at lower pH (see Figure 8a for an example within the Cl-HT system, and Supplementary Information: Figure S5 for the Br-HT and I-HT systems). The formation of the anion-containing hydrotalcites is predicted to be suppressed by the formation of OH-HT phases at higher pH due to the decreasing anion/OH ratio in the solution. This may suggest that HT3 phases have a narrow range of stability, but may also suggest a need for reconfirming thermochemical data for the OH-HT compounds. The phases synthesized here are not perfectly aligned with the initial target composition (Mg/Al = 2 and 3) and the range of stability of each anion-containing hydrotalcite varies: e.g., Br-HT phase stability is observed to prevail over Cl-HT and I-HT when anions are introduced in equimolar content in solution (total anion concentration = 1 M, Figure 8b), and all phases are dominated by OH-HT at higher pH. Nonetheless, the solid solutions obtained here still show a competitive effect as a function of anion ratio at fixed pH (total anion concentration = 1 M at pH 11.5 – approaching a cement pore solution[46] – Figure 8c). All HT phases form, but the Br-HT phase is prevalent even when Br is the minor anion in solution as compared to Cl and/or I. The order of preferential phase formation thus is Br > Cl > I, which is similar to the order of preferential incorporation observed by Bontchev et *al.*[19] However, in contrast with the results of Bontchev et *al.*, here, very little to no mixed-phase formation is observed in Figure 8c (i.e., a mixed-halide system). This suggests that hydrotalcite phases may not be the most appropriate type of cementitious phases to encapsulate mixed-anion wastes containing multiple halides, particularly where the primary anion of interest is present at lower concentration than a less-hazardous anion (e.g., radioiodine at low concentrations in a chloride brine). In addition, the stability of the phases presented above is valid within a simple MgO-Al_2O_3-MgX_2-H_2O system (where X = Cl, Br, and/or I). In more

complex cementitious systems where excess Ca content (e.g., as portlandite) is typically present, hydrotalcite phases are in competition with other hydrates such as C-S-H and/or AFm and AFt phases that are more likely to form,[15] while hydrotalcite phases usually form in systems with high Mg and Al content (e.g., slags containing cement system, alkali activated slags, etc.).[72,73]

For AFm phases, all of the halide-containing phases are observed to be more stable than solely OH-containing calcium aluminate phases (e.g., OH-AFm, C_3AH_6)[36] up to very high pH (see Figure 8d for an example within the Cl-AFm system, and Supplementary Information: Figure S5 for the Br-AFm and I-AFm systems). In contrast to hydrotalcite phases, Cl- and Br-AFm phases coexist when anions are introduced at equimolar content in solution, but I-AFm formation is still suppressed (total anion concentration = 1 M, Figure 8e). This is further observed in Figure 8f where Br-AFm forms preferentially over I-AFm and Cl-AFm in a mixed-anion solution at pH 12, while I-AFm appears to be the least stable AFm phase in mixed-anion solutions. This trend follows the ordering of the logK_{SO} values for the AFm phases: Br-AFm < Cl-AFm < I-AFm (i.e., a more negative logK_{SO} indicates more thermodynamically stable phase formation) and is consistent with the trend observed for hydrotalcite phases. Regardless, AFm phases show a higher propensity to encapsulate mixed anions, e.g., brines containing multiple halide elements, although iodide may remain a challenge if its content is too low vis-à-vis other halide species. In complex cementitious systems, AFm phases may compete with other Ca-containing hydrate phases, notably C-S-H and AFt phases,[74–77] yet they have been observed to form alongside these phases.[8,16,17] It is thus likely that the phases studied herein may form alongside typical cement hydrates, provided that sufficient excess Ca and Al is available from clinker reaction over time.

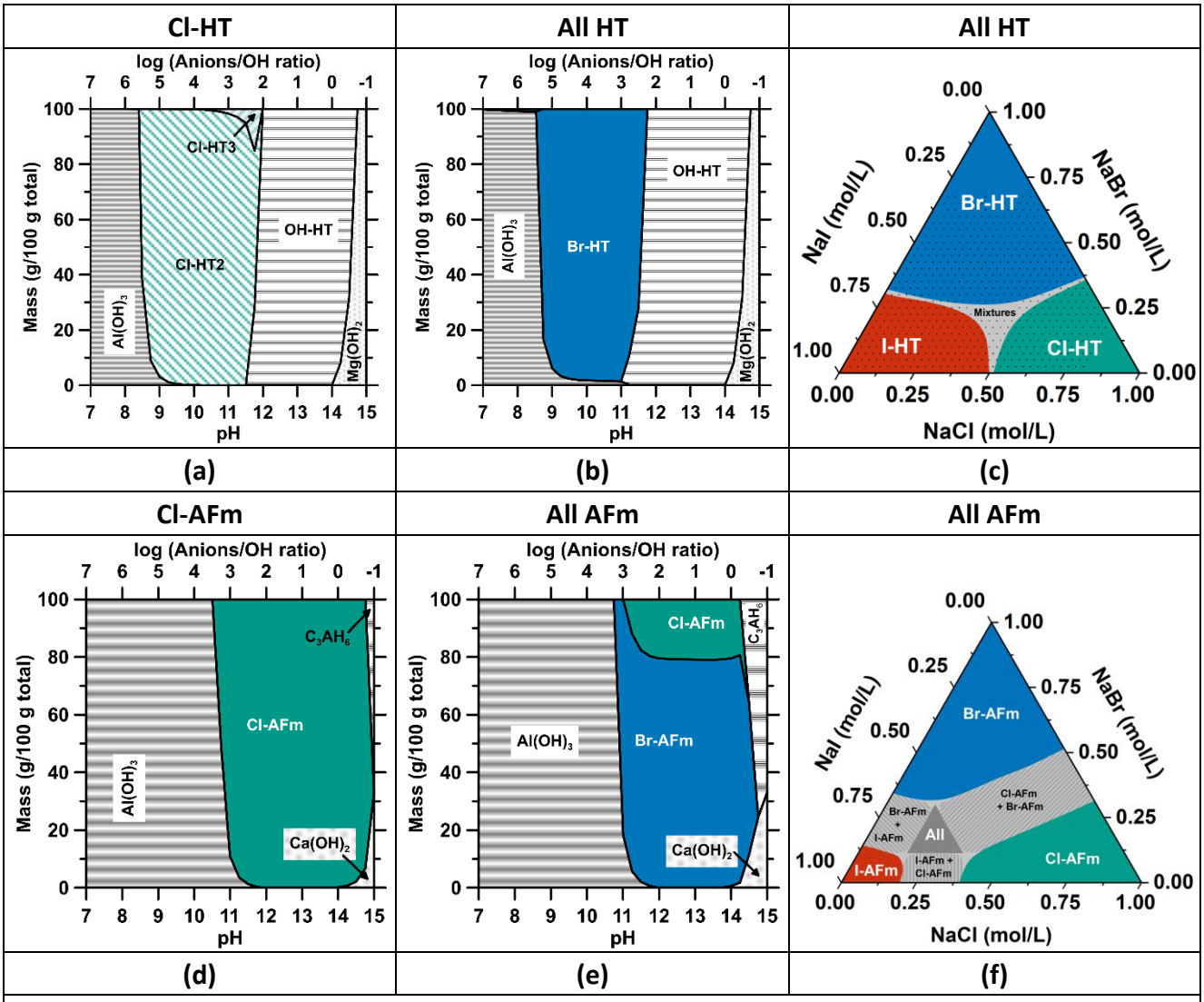

Figure 8. Thermodynamic modeling of a 0.01 M Al_2O_3 + 0.05 M MgO system with (a) a 1 M NaCl solution as a function of pH, (b) a 1 M equimolar [NaCl + NaBr + NaI] solution as a function of pH, (c) various NaX concentration (X = Cl, Br, and/or I) at pH 11.5. The dotted areas highlight the concentration range where OH-HT was also observed to form. The thermodynamic modeling of a 0.1 M Al_2O_3 + 0.4 M CaO system with (d) a 1 M NaCl solution as a function of pH, (e) a 1 M equimolar [NaCl + NaBr + NaI] solution as a function of pH, and (f) various NaX concentration (X = Cl, Br, and/or I) at pH 12.0.

SUMMARY AND CONCLUSIONS

The thermochemical data of synthetic LDH compounds of general formula $[M^{II}_{(1-x)}M^{III}_{(x)}(OH)_2][A^{n-}]_{x/n}\cdot zH_2O$ were determined. Solids were synthesized with A = Cl^-, Br^-, or I^-, M^{III} = Al, and M^{II} = Mg (hydrotalcite) or Ca (AFm). The target compositions were $[M^{II}/Al]$ = 2 (Ca and Mg, atomic units) or 3

(Mg only). The composition, crystallinity, and water content of all phases were determined from a combination of acid digestion, XRD, and TGA analysis. The solubility constants of hydrotalcite phases were found to be sensitive to the Mg/Al ratio for hydrotalcite phases, following a linear relationship. A limited effect of the anion is observed on the solubility value, with differences observed to be less than ± 2 log units. For AFm phases, where the experimental composition is similar to the target composition, the solubility constants at 25 °C of these phases were found to decrease in the order Br^- < Cl^- < I^-. The solubility data were used to calculate the stability fields of these phases versus other phases of interest. In general, the anion-containing hydrotalcite's range of stability is at lower pH (9 to 11.5) than the AFm phases (11 to 15). Hydrotalcite phases have to compete with meixnerite (hydroxy-hydrotalcite) at higher pH, while AFm phases are shown to be stable even with increasing pH. In general, for both HT and AFm phases, the preferential order of formation of the phases is Br > Cl > I, which is consistent with previous observations. This work provides new insights regarding hydrotalcite and/or AFm phases formation in carbonate-free cementitious systems, that may be used in management of halide-containing liquid wastes.

ACKNOWLEDGMENTS

The authors acknowledge financial support for this research provided by the Electric Power Research Institute (EPRI). The contents of this paper reflect the views and opinions of the authors, who are responsible for the accuracy of data presented herein. This research was conducted in the Laboratory for the Chemistry of Construction Materials (LC^2) and the Molecular Instrumentation Center (MIC) at the University of California, Los Angeles (UCLA). As such, the authors acknowledge the support that has

made these laboratories and their operations possible. The authors would also like to thank Barbara Lothenbach and Elina Bernard for scientific discussions.

REFERENCES

1. Prentice, D. P., Bernal, S. A., Bankhead, M., Hayes, M. & Provis, J. L. Phase evolution of slag-rich cementitious grouts for immobilisation of nuclear wastes. *Adv. Cem. Res.* **30**, 345–360 (2018).
2. Prentice, D. P. *et al.* Thermodynamic modelling of BFS-PC cements under temperature conditions relevant to the geological disposal of nuclear wastes. *Cem. Concr. Res.* **119**, 21–35 (2019).
3. Kearney, S. *et al.* Cement-based stabilization/solidification of radioactive waste. in *Low Carbon Stabilization and Solidification of Hazardous Wastes* 407–431 (Elsevier, 2022). doi:10.1016/B978-0-12-824004-5.00005-0.
4. Shi, C. & Day, R. L. *Alkali-slag cements for the immobilization of radioactive wastes*. (1996).
5. Cath, T. *et al. National Alliance for Water Innovation (NAWI) Technology Roadmap: Industrial Sector*. DOE/GO-102021-5562 https://www.nrel.gov/docs/fy21osti/79886.pdf (2021).
6. Matschei, T., Lothenbach, B. & Glasser, F. P. The AFm phase in Portland cement. *Cem. Concr. Res.* **37**, 118–130 (2007).
7. Gougar, M. L. D., Scheetz, B. E. & Roy, D. M. Ettringite and C-S-H Portland cement phases for waste ion immobilization: A review. *Waste Manag.* **16**, 295–303 (1996).
8. Balonis, M., Lothenbach, B., Le Saout, G. & Glasser, F. P. Impact of chloride on the mineralogy of hydrated Portland cement systems. *Cem. Concr. Res.* **40**, 1009–1022 (2010).
9. Bernard, E., Zucha, W. J., Lothenbach, B. & Mäder, U. Stability of hydrotalcite (Mg-Al layered double hydroxide) in presence of different anions. *Cem. Concr. Res.* **152**, 106674 (2022).

10. Mills, S. J., Christy, A. G., Génin, J.-M. R., Kameda, T. & Colombo, F. Nomenclature of the hydrotalcite supergroup: natural layered double hydroxides. *Mineral. Mag.* **76**, 1289–1336 (2012).
11. Rives, V. Characterisation of layered double hydroxides and their decomposition products. *Mater. Chem. Phys.* **75**, 19–25 (2002).
12. Rives, V. & Ulibarri, M. A. Layered double hydroxides (LDH) intercalated with metal coordination compounds and oxometalates. *Coord. Chem. Rev.* **181**, 61–120 (1999).
13. Constantino, V. R. L. & Pinnavaia, T. J. Basic Properties of $Mg_{2+1-x}Al_{3+x}$ Layered Double Hydroxides Intercalated by Carbonate, Hydroxide, Chloride, and Sulfate Anions. *Inorg. Chem.* **34**, 883–892 (1995).
14. Richardson, I. G. Clarification of possible ordered distributions of trivalent cations in layered double hydroxides and an explanation for the observed variation in the lower solid-solution limit. *Acta Crystallogr. Sect. B Struct. Sci. Cryst. Eng. Mater.* **69**, 629–633 (2013).
15. Prentice, D. P. *et al.* The effects of (di-,tri-valent)-cation partitioning and intercalant anion-type on the solubility of hydrotalcites. *J. Am. Ceram. Soc.* **103**, 6025–6039 (2020).
16. Collin, M. *et al.* Fly Ash–$Ca(OH)_2$ Reactivity in Hypersaline NaCl and $CaCl_2$ Brines. *ACS Sustain. Chem. Eng.* **9**, 8561–8571 (2021).
17. Collin, M. *et al.* How Brine Composition Affects Fly Ash Reactions: The Influence of (Cat-, An-)ion Type. *Adv. Civ. Eng. Mater.* **11**, 20210155 (2022).
18. Miyata, S. Anion-Exchange Properties of Hydrotalcite-Like Compounds. *Clays Clay Miner.* **31**, 305–311 (1983).

19. Bontchev, R. P., Liu, S., Krumhansl, J. L., Voigt, J. & Nenoff, T. M. Synthesis, Characterization, and Ion Exchange Properties of Hydrotalcite $Mg_6Al_2(OH)_{16}(A)_x(A')_{2-x}\cdot 4H_2O$ (A, A' = Cl^-, Br^-, I^-, and NO_3^-, $2 \geq x \geq 0$) Derivatives. *Chem. Mater.* **15**, 3669–3675 (2003).
20. He, J. *et al.* Preparation of Layered Double Hydroxides. in *Layered Double Hydroxides* (eds. Duan, X. & Evans, D. G.) vol. 119 89–119 (Springer-Verlag, 2006).
21. Teodorescu, F., Pălăduţă, A.-M. & Pavel, O. D. Memory effect of hydrotalcites and its impact on cyanoethylation reaction. *Mater. Res. Bull.* **48**, 2055–2059 (2013).
22. Kovanda, F., Koloušek, D., Cílová, Z. & Hulínský, V. Crystallization of synthetic hydrotalcite under hydrothermal conditions. *Appl. Clay Sci.* **28**, 101–109 (2005).
23. Allada, R. K., Pless, J. D., Nenoff, T. M. & Navrotsky, A. Thermochemistry of Hydrotalcite-like Phases Intercalated with CO_3^{2-}, NO_3^-, Cl^-, I^-, and ReO_4^-. *Chem. Mater.* **17**, 2455–2459 (2005).
24. Balonis, M., Mędala, M. & Glasser, F. P. Influence of calcium nitrate and nitrite on the constitution of AFm and AFt cement hydrates. *Adv. Cem. Res.* **23**, 129–143 (2011).
25. Birnin-Yauri, U. A. & Glasser, F. P. Friedel's salt, $Ca_2Al(OH)_6(Cl,OH)\cdot 2H_2O$: its solid solutions and their role in chloride binding. *Cem. Concr. Res.* **28**, 1713–1723 (1998).
26. Mesbah, A. *et al.* Crystal structure of Kuzel's salt $3CaO\cdot Al_2O_3\cdot 1/2CaSO_4\cdot 1/2CaCl_2\cdot 11H_2O$ determined by synchrotron powder diffraction. *Cem. Concr. Res.* **41**, 504–509 (2011).
27. Lothenbach, B., Durdziński, P. T. & De Weerdt, K. Thermogravimetric analysis. in *A practical guide to Microstructural analysis of cementitious materials* (2016).
28. Shi, Z. *et al.* Friedel's salt profiles from thermogravimetric analysis and thermodynamic modelling of Portland cement-based mortars exposed to sodium chloride solution. *Cem. Concr. Compos.* **78**, 73–83 (2017).

29. Laugier, J. & Bochu, B. *LMGP-Suite Suite of Programs for the interpretation of X-ray Experiments, ENSP/Laboratoire des Matériaux et du Génie Physique BP 46. 38042 Saint Martin d'Hères, France*. http://www.inpg.fr/LMGP and http://www.ccp14.ac.uk/tutorial/lmgp/.
30. Damidot, D., Lothenbach, B., Herfort, D. & Glasser, F. P. Thermodynamics and cement science. *Cem. Concr. Res.* **41**, 679–695 (2011).
31. Shock, E. L., Sassani, D. C., Willis, M. & Sverjensky, D. A. Inorganic species in geologic fluids: Correlations among standard molal thermodynamic properties of aqueous ions and hydroxide complexes. *Geochim. Cosmochim. Acta* **61**, 907–950 (1997).
32. Johnson, J. W., Oelkers, E. H. & Helgeson, H. C. SUPCRT92: A software package for calculating the standard molal thermodynamic properties of minerals, gases, aqueous species, and reactions from 1 to 5000 bar and 0 to 1000 °C. *Comput. Geosci.* **18**, 899–947 (1992).
33. Robie, R. A. & Hemingway, B. S. *Thermodynamic properties of minerals and related substances at 298.15 K and 1 bar (10^5 pascals) pressure and at higher temperatures*. U.S. Geological Survey Bulletin 2131. Washington: U.S.G.S. (1995) doi:10.3133/b2131.
34. Helgeson, H. C., Delany, J., Nesbitt, H. W. & Bird, D. K. Summary and critique of the thermodynamic properties of rock forming minerals. *Am. J. Sci.* **278-A**, 1–229 (1978).
35. Hummel, W., Berner, U., Curti, E., Pearson, F. J. & Thoenen, T. Nagra/PSI Chemical Thermodynamic Data Base 01/01. *Radiochim. Acta* **90**, 805–813 (2002).
36. Lothenbach, B., Pelletier-Chaignat, L. & Winnefeld, F. Stability in the system $CaO–Al_2O_3–H_2O$. *Cem. Concr. Res.* **42**, 1621–1634 (2012).
37. Kondepudi, D. & Prigogine, I. *Modern Thermodynamics: From Heat Engines to Dissipative Structures*. (Wiley, 2014). doi:10.1002/9781118698723.

38. Chase, M. W. *NIST-JANAF thermochemical tables*. (American Chemical Society ; American Institute of Physics for the National Institute of Standards and Technology, 1998).
39. Lange, N. A. *Lange's handbook of chemistry*. (McGraw-Hill, 1979).
40. Anderson, G. M. & Crerar, D. A. *Thermodynamics in geochemistry: the equilibrium model*. (Oxford University Press, 1993).
41. Kulik, D. A. *et al.* GEM-Selektor geochemical modeling package: revised algorithm and GEMS3K numerical kernel for coupled simulation codes. *Comput. Geosci.* 1–24 (2012) doi:10.1007/s10596-012-9310-6.
42. Wagner, T., Kulik, D. A., Hingerl, F. F. & Dmytrieva, S. V. GEM-Selektor geochemical modeling package: TSolMod library and data interface for multicomponent phase models. *Can. Mineral.* **50**, 1173–1195 (2012).
43. Thoenen, T., Hummel, W., Berner, U. & Curti, E. *The PSINagra chemical thermodynamic database 12/07*. PSI-Bericht Nr 14-04. Villigen: Paul Scherrer Institut (2014).
44. Lothenbach, B. *et al.* Cemdata18: A chemical thermodynamic database for hydrated Portland cements and alkali-activated materials. *Cem. Concr. Res.* **115**, 472–506 (2019).
45. Helgeson, H. C., Kirkham, D. H. & Flowers, G. C. Theoretical prediction of the thermodynamic behavior of aqueous electrolytes by high pressures and temperatures; IV, Calculation of activity coefficients, osmotic coefficients, and apparent molal and standard and relative partial molal properties to 600 °C and 5 kb. *Am. J. Sci.* **281**, 1249–1516 (1981).
46. Vollpracht, A., Lothenbach, B., Snellings, R. & Haufe, J. The pore solution of blended cements: a review. *Mater. Struct.* **49**, 3341–3367 (2016).

47. Miyata, S. The Syntheses of Hydrotalcite-Like Compounds and Their Structures and Physico-Chemical Properties I: The Systems $Mg^{2+}Al^{3+}$-NO^{3-}, Mg^{2+}-Al^{3+}-Cl^{-}, Mg^{2+}-Al^{3+}-ClO_4^{-}, Ni^{2+}-Al^{3+}-Cl^{-} and Zn^{2+}-Al^{3+}-Cl^{-}. *Clays Clay Miner.* **23**, 369–375 (1975).
48. Rozov, K. *et al.* Synthesis and characterization of the LDH hydrotalcite–pyroaurite solid-solution series. *Cem. Concr. Res.* **40**, 1248–1254 (2010).
49. Renaudin, G., Kubel, F., Rivera, J.-P. & Francois, M. Structural phase transition and high temperature phase structure of Friedels salt, 3CaO · Al2O3 · CaCl2 · 10H2O. *Cem. Concr. Res.* **29**, 1937–1942 (1999).
50. Malani, A., Murad, S. & Ayappa, K. G. Hydration of ions under confinement. *Mol. Simul.* **36**, 579–589 (2010).
51. Marcus, Y. Ionic radii in aqueous solutions. *Chem. Rev.* **88**, 1475–1498 (1988).
52. Cavani, F., Trifirò, F. & Vaccari, A. Hydrotalcite-type anionic clays: Preparation, properties and applications. *Catal. Today* **11**, 173–301 (1991).
53. Curti, E. Coprecipitation of radionuclides with calcite : estimation of partition coefficients based on a review of laboratory investigations and geochemical data. *Appl. Geochem.* **14**, 433–445 (1999).
54. Shannon, R. D. Revised effective ionic radii and systematic studies of interatomic distances in halides and chalcogenides. *Acta Crystallogr. Sect. A* **32**, 751–767 (1976).
55. Ahrens, L. H. The use of ionization potentials Part 1. Ionic radii of the elements. *Geochim. Cosmochim. Acta* **2**, 155–169 (1952).
56. Runčevski, T., Dinnebier, R. E., Magdysyuk, O. V. & Pöllmann, H. Crystal structures of calcium hemicarboaluminate and carbonated calcium hemicarboaluminate from synchrotron powder diffraction data. *Acta Crystallogr. B* **68**, 493–500 (2012).

57. Richardson, I. G. The importance of proper crystal-chemical and geometrical reasoning demonstrated using layered single and double hydroxides. *Acta Crystallogr. Sect. B Struct. Sci. Cryst. Eng. Mater.* **69**, 150–162 (2013).
58. Hu, G. & O'Hare, D. Unique Layered Double Hydroxide Morphologies Using Reverse Microemulsion Synthesis. *J. Am. Chem. Soc.* **127**, 17808–17813 (2005).
59. Wu, Q., Olafsen, A., Vistad, Ø. B., Roots, J. & Norby, P. Delamination and restacking of a layered double hydroxide with nitrate as counter anion. *J. Mater. Chem.* **15**, 4695 (2005).
60. Balonis, M. & Glasser, F. P. The density of cement phases. *Cem. Concr. Res.* **39**, 733–739 (2009).
61. Rapin, J.-P. & François, M. The double-layered hydroxide $3CaO{\cdot}Al_2O_3{\cdot}0.5CaBr_2{\cdot}0.5CaCl_2{\cdot}10H_2O$. *Acta Crystallogr. C* **57**, 137–138 (2001).
62. Rapin, J.-P., Walcarius, A., Lefevre, G. & François, M. A double-layered hydroxide, $3CaO.Al_2O_3.CaI_2.10H_2O$. *Acta Crystallogr. C* **55**, 1957–1959 (1999).
63. Nedyalkova, L., Lothenbach, B., Geng, G., Mäder, U. & Tits, J. Uptake of iodide by calcium aluminate phases (AFm phases). *Appl. Geochem.* **116**, 104559 (2020).
64. Nedyalkova, L. *et al.* Mechanisms and thermodynamic modelling of iodide sorption on AFm phases. *J. Colloid Interface Sci.* **608**, 683–691 (2022).
65. Pauling, L. *The nature of the chemical bond and the structure of molecules and crystals: an introduction to modern structural chemistry*. (Cornell Univ. Press, 2010).
66. Renaudin, G., Rapin, J.-P., Elkaim, E. & François, M. Polytypes and polymorphs in the related Friedel's salt $[Ca_2Al(OH)_6]+[X{\cdot}2H_2O]-$ halide series. *Cem. Concr. Res.* **34**, 1845–1852 (2004).
67. Pöllmann, H. The crystal chemistry of $C_3(A,F){\cdot}CaX{\cdot}nH_2O$. in *Cementitious Materials: Composition, Properties, Application* (De Gruyter, 2017). doi:10.1515/9783110473728.

68. Terzis, A., Filippakis, S., Kuzel, H.-J. & Burzlaff, H. The crystal structure of $Ca_2Al(OH)_6Cl \cdot 2H_2O$. *Z. Für Krist. - Cryst. Mater.* **181**, 29–34 (1987).
69. Theiss, F. L., Ayoko, G. A. & Frost, R. L. Thermogravimetric analysis of selected layered double hydroxides. *J. Therm. Anal. Calorim.* **112**, 649–657 (2013).
70. Liang, L. & Li, L. Adsorption behavior of calcined layered double hydroxides towards removal of iodide contaminants. *J. Radioanal. Nucl. Chem.* **273**, 221–226 (2007).
71. Renaudin, G., Mesbah, A., Dilnesa, B., Francois, M. & Lothenbach, B. Crystal Chemistry of Iron Containing Cementitious AFm Layered Hydrates. *Curr. Inorg. Chem.* **5**, 184–193 (2015).
72. Ben Haha, M., Le Saout, G., Winnefeld, F. & Lothenbach, B. Influence of activator type on hydration kinetics, hydrate assemblage and microstructural development of alkali activated blast-furnace slags. *Cem. Concr. Res.* **41**, 301–310 (2011).
73. Lothenbach, B. & Gruskovnjak, A. Hydration of alkali-activated slag: thermodynamic modelling. *Adv. Cem. Res.* **19**, 81–92 (2007).
74. Lothenbach, B., Matschei, T., Möschner, G. & Glasser, F. P. Thermodynamic modelling of the effect of temperature on the hydration and porosity of Portland cement. *Cem. Concr. Res.* **38**, 1–18 (2008).
75. Lothenbach, B. Thermodynamic equilibrium calculations in cementitious systems. *Mater. Struct.* **43**, 1413–1433 (2010).
76. Lothenbach, B. & Zajac, M. Application of thermodynamic modelling to hydrated cements. *Cem. Concr. Res.* **123**, 105779 (2019).

77. Matschei, T., Lothenbach, B. & Glasser, F. P. Thermodynamic properties of Portland cement hydrates in the system $CaO–Al_2O_3–SiO_2–CaSO_4–CaCO_3–H_2O$. *Cem. Concr. Res.* **37**, 1379–1410 (2007).

SUPPLEMENTARY INFORMATION

Table S1. Thermodynamic properties of the solid and aqueous constituents used to calculate $\Delta_f G^\circ_{298}$, $\Delta_f H^\circ_{298}$, $\Delta_f S^\circ_{298}$ and Cp°_{298} for the hydrotalcite phases. Reference state of 298.15 K and 1 bar.

Species	$\Delta_f \boldsymbol{G}^\circ_{\boldsymbol{298}}$	$\Delta_f \boldsymbol{H}^\circ_{\boldsymbol{298}}$	$\boldsymbol{S}^\circ_{\boldsymbol{298}}$	$\boldsymbol{Cp}^\circ_{\boldsymbol{298}}$	**Ref**
	(kJ·mol−1)	(kJ·mol−1)	(J·mol−1)	(J·mol−1·K−1)	
Solids					
$Ca(OH)_2$	-897.01	-984.68	83.40	87.51	[36]
$Mg(OH)_2$	-832.23	-923.27	63.14	77.28	[36]
$Al(OH)_3$ (microcrystalline)	-1150.99	-1288.72	70.08	93.08	[36]
$CaCl_2$	-747.70	-795.80	104.60	72.83	[33]
$CaBr_2$	-663.60	-682.80	130.00	75.00	[37,38]
CaI_2	-533.13	-536.81	145.27	77.16	[38,39]
$MgCl_2$	-591.80	-641.30	89.60	71.04	[33]
$MgBr_2$	-503.80	-524.30	117.20	73.16	[37,38]
MgI_2	-358.15	-364.01	127.70	74.81	[38,39]
Aqueous constituents					
Ca^{2+}	-552.79	-543.07	-56.48	-30.92	[31]
Mg^{2+}	-453.99	-465.93	-138.07	-21.66	[31]
AlO_2^-	-827.48	-925.57	-30.21	-49.04	[31]
OH^-	-157.27	-230.01	-10.71	-136.34	[31]
Cl^-	-131.29	-167.11	58.41	-122.49	[31]
Br^-	-104.06	-121.53	82.84	-126.63	[31]
I^-	-51.92	-56.91	106.69	-117.57	[31]
$H_2O°$	-237.18	-285.88	69.92	75.36	[32]

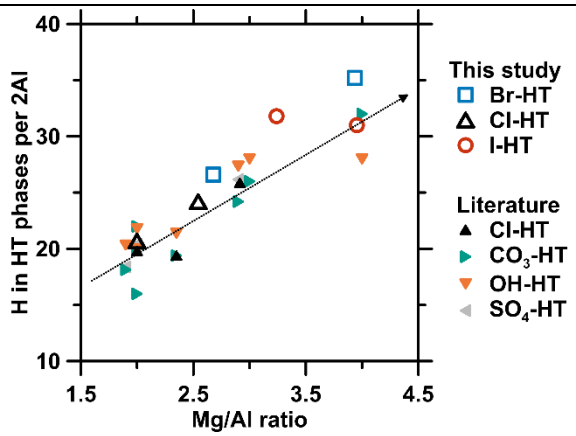

Figure S1. The comparison between the total amount of hydrogen (as water molecule and hydroxyl species) within the HT phases synthesized herein and the Mg/Al ratio, compared to that measured for other phases presented in the literature.

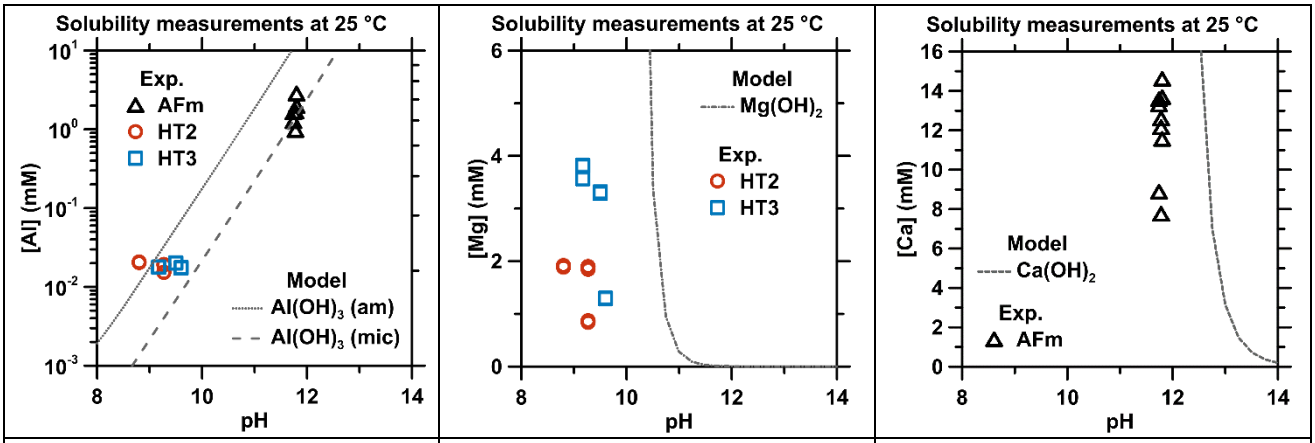

Figure S2. The experimental concentration of (a) Al, (b) Mg, and (c) Ca after 5 months of equilibration of the synthesized solids in DIW at 25 °C compared to the solubility limit of $Al(OH)_3$ (amorphous and microcrystalline), $Mg(OH)_2$, and $Ca(OH)_2$ respectively as implemented in GEMS.

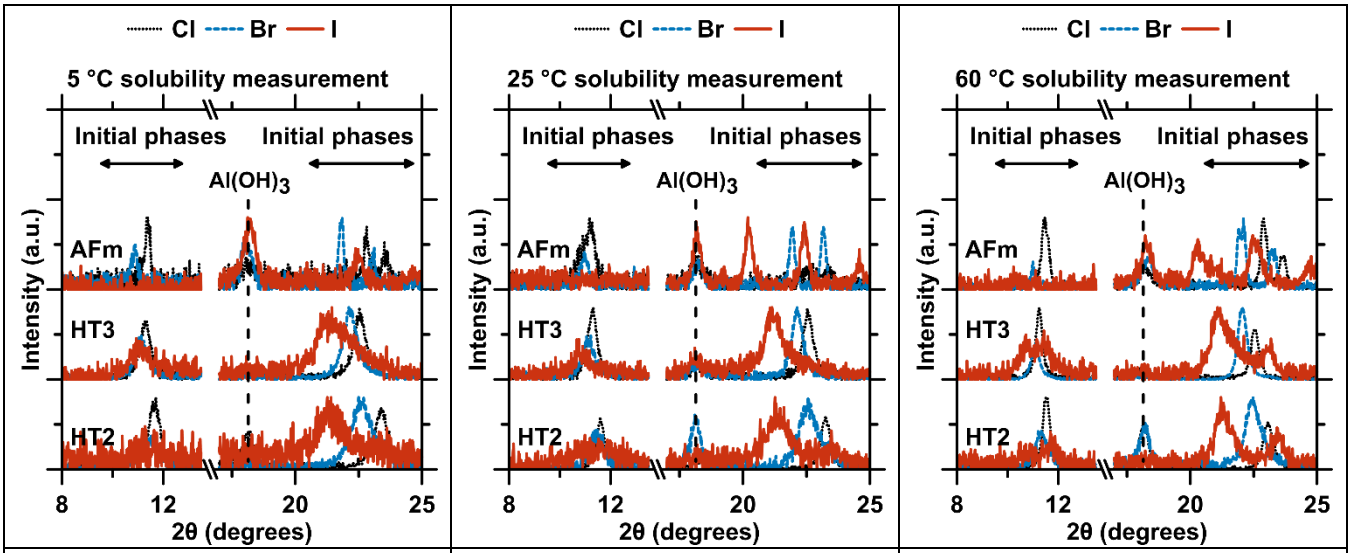

Figure S3. XRD pattern of the solids retrieved after the solubility experiment at **(a)** 5 °C, **(b)** 25 °C, and **(c)** 60 °. The only solids identified are the phases initially introduced, and poorly crystalline $Al(OH)_3$. Note that in all cases, the low amount of solid retrieved and the contamination with PTFE particulates scraped from the container made it challenging to obtain a satisfactory signal.

Table S2. Average solution composition of all phases equilibrated for 5 months at 5, 25, and 60 °C. Concentrations are given in mmol/L.

Equilibrated AFm solutions								
Sample Id	**T (°C)**	**Al**	**Ca**	**Cl**	**I**	**Br**	**pH at T °C**	**Log K_{so}**
Cl-AFm	5	2.58	9.42	11.42	-	-	12.06	-29.3
	25	1.65	11.92	8.43	-	-	11.74	-27.7
	60	2.61	16.44	18.83	-	-	11.00	-26.0
Br-AFm	5	2.66	9.28	-	-	7.22	11.96	-30.2
	25	1.22	10.84	-	-	12.50	11.78	-28.1
	60	2.42	18.78	-	-	19.63	10.90	-26.3
I-AFm	5	2.76	11.52	-	15.90	-	12.03	-28.8
	25	2.57	13.29	-	19.82	-	11.80	-26.7
	60	2.58	25.69	-	42.67	-	10.82	-25.6
Equilibrated HT solutions								
Sample Id	**T (°C)**	**Al**	**Mg**	**Cl**	**I**	**Br**	**pH at T °C**	**Log K_{so}**
Cl-HT2	5	2.97×10^{-2}	24.59	51.06	-	-	8.20	-61.3
	25	1.54×10^{-2}	3.11	8.96	-	-	9.27	-56.4
	60	1.96×10^{-2}	3.02	7.18	-	-	8.57	-54.8
Cl-HT3	5	1.72×10^{-2}	8.11	18.61	-	-	9.80	-81.2
	25	1.78×10^{-2}	6.15	15.08	-	-	9.17	-81.0
	60	1.92×10^{-2}	6.82	16.89	-	-	8.86	-74.2
Br-HT2	5	2.46×10^{-2}	1.52	-	-	3.02	9.80	-64.4
	25	1.91×10^{-2}	1.41	-	-	3.10	9.27	-63.5
	60	1.89×10^{-2}	2.01	-	-	4.32	8.70	-60.0
Br-HT3	5	1.80×10^{-2}	4.48	-	-	7.48	9.99	-90.9
	25	2.01×10^{-2}	5.45	-	-	9.13	9.50	-87.3
	60	1.65×10^{-2}	5.35	-	-	8.93	9.20	-79.9
I-HT2	5	1.79×10^{-2}	0.50	-	1.04	-	10.37	-77.8
	25	2.06×10^{-2}	3.14	-	7.30	-	8.80	-74.4
	60	1.71×10^{-2}	3.20	-	7.14	-	9.10	-68.4
I-HT3	5	1.76×10^{-2}	1.51	-	3.69	-	10.32	-94.4
	25	1.75×10^{-2}	2.13	-	5.09	-	9.60	-93.0
	60	2.36×10^{-2}	6.21	-	14.18	-	9.20	-82.3

Table S3. The error propagation analysis that is used to assess the uncertainty in the solubility constant that is derived from measured solution concentration data.

The solubility constants of AFm phases and HT phases are calculated using the following equation:

$$\log \mathrm{K_{so}} = \sum \log \mathrm{a_x} \cdot \mathrm{n} \qquad \text{Equation A}$$

where K_{SO} is the solubility constant, a_x is the activity of a given ionic species and n its stoichiometric coefficient. As a result, the associated standard deviation/uncertainty in the solubility constant may be calculated via error propagation considering the following equation:

$$\Delta \log K_{so} = \sqrt{\sum \left[\log a_x \cdot n \sqrt{\left(\frac{\Delta \log a_x}{\log \mathrm{a_x}}\right)^2 + \left(\frac{\Delta \mathrm{n}}{\mathrm{n}}\right)^2} \right]^2} \qquad \text{Equation B}$$

The uncertainty considered for the activity and the stoichiometric coefficient are detailed below:

Solids: The uncertainty associated with the solid composition, and in turn the stoichiometric coefficient is linked to the uncertainty in the estimated solid composition as noted below.

	Al	**Ca**	**Cl**	**I**	**Br**	**OH^-**	**H_2O**
All phases	10% from average error propagation observed on all solids						

Solution: The uncertainty associated with the ion activities is linked to the uncertainty in the measured solution concentrations as noted below.

	Al	**Ca**	**Cl**	**I**	**Br**	**OH^-**	**H_2O**
All phases	Standard deviation of three measurements					2.3%*	N.A.

* based on an uncertainty in the pH measurement for a calibrated pH meter of ±0.01 units.

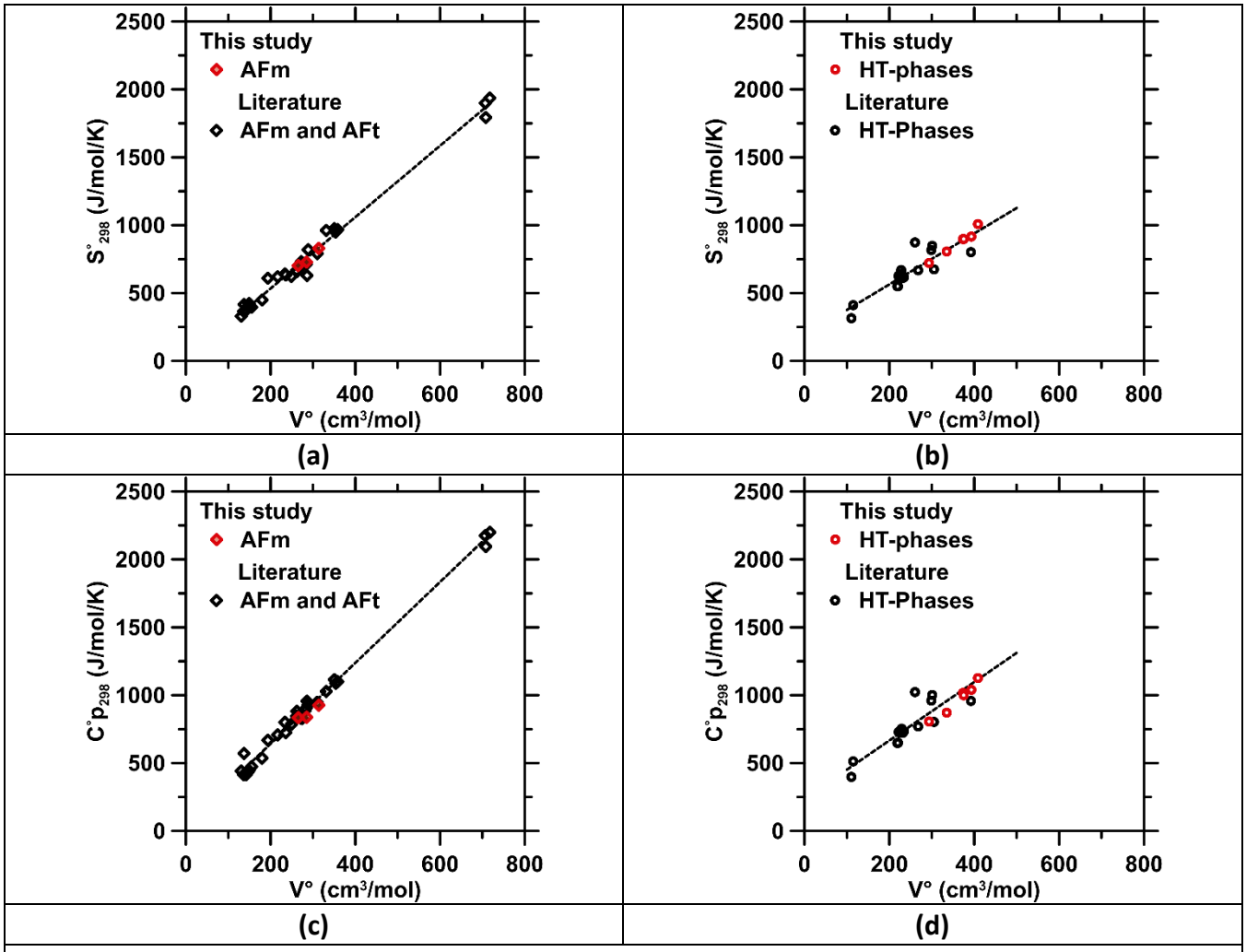

Figure S4. A comparison between the thermodynamic properties of the phases synthesized herein, and that of others calcium and magnesium aluminate mineral hydrates from the slop98.dat and Cemdata18 thermodynamic databases[9,15,32,35,43,44,74] showing comparisons for: Entropy (S°_{298}) of **(a)** AFm and **(b)** HT phases, and Heat capacity ($C^{\circ}p_{298}$) of **(c)** AFm and **(d)** HT phases as a function of the experimental molar volume V°.

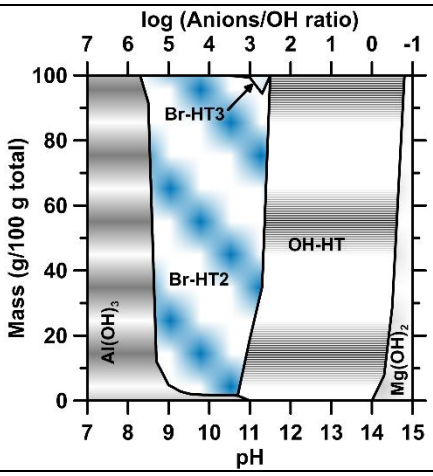

(a)

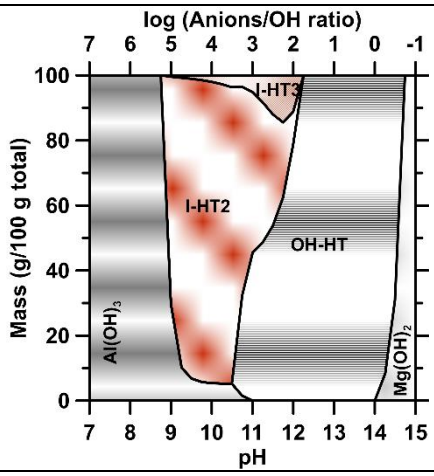

(b)

Figure S5. The thermodynamic modeling of a 0.01 M Al_2O_3 + 0.05 M MgO system with **(a)** a 1 M NaBr solution, and **(b)** a 1 M NaI solution as a function of pH.

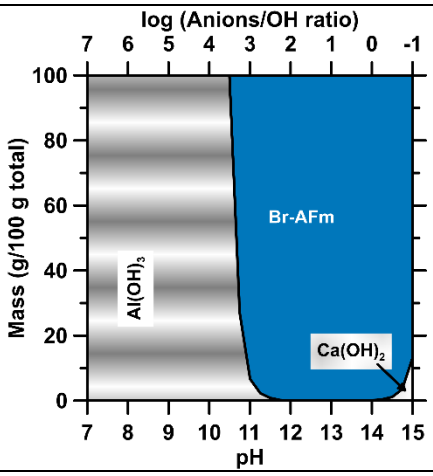

(a)

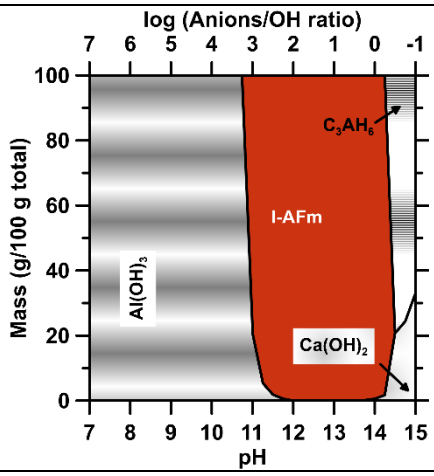

(b)

Figure S6. The thermodynamic modeling of a 0.01 M Al_2O_3 + 0.04 M CaO system with **(a)** a 1 M NaBr solution, and **(b)** a 1 M NaI solution as a function of pH.